

A Photometric and Kinematic Study of AWM 7¹

Daniel M. Koranyi and Margaret J. Geller
 Harvard-Smithsonian Center for Astrophysics

Joseph J. Mohr
 Dept. of Physics, University of Michigan

Gary Wegner
 Dept. of Physics & Astronomy, Dartmouth College

ABSTRACT

We have measured redshifts and Kron-Cousins R -band magnitudes for a sample of galaxies in the poor cluster AWM 7. We have measured redshifts for 172 galaxies; 106 of these are cluster members. We determine the luminosity function from a photometric survey of the central $1.2 h^{-1} \times 1.2 h^{-1}$ Mpc. The LF has a bump at the bright end and a faint-end slope of $\alpha = -1.37 \pm 0.16$, populated almost exclusively by absorption-line galaxies. The cluster velocity dispersion is lower in the core (~ 530 km s $^{-1}$) than at the outskirts (~ 680 km s $^{-1}$), consistent with the cooling flow seen in the X-ray. The cold core extends $\sim 150 h^{-1}$ kpc from the cluster center. The Kron-Cousins R -band mass-to-light ratio of the system is $650 \pm 170 h M_{\odot}/L_{\odot}$, substantially lower than previous optical determinations, but consistent with most previous X-ray determinations. We adopt $H_0 = 100 h$ km s $^{-1}$ Mpc $^{-1}$ throughout this paper; at the mean cluster redshift, $(5247 \pm 76$ km s $^{-1}$), $1 h^{-1}$ Mpc subtends 65.5.

Subject headings: galaxies: clusters: individual (AWM 7) — galaxies: luminosity function, mass function

¹ Observations reported in this paper were obtained at the MDM Observatory, a facility jointly operated by the University of Michigan, Dartmouth College, and the Massachusetts Institute of Technology; at the Multiple Mirror Telescope Observatory, a facility operated jointly by the University of Arizona and the Smithsonian Institution; and at the Whipple Observatory, a facility operated jointly by the Smithsonian Astrophysical Observatory and Harvard University.

1. Introduction

The AWM and MKW clusters were selected on the basis of the appearance of the central cD galaxy (Morgan *et al.* 1975, Albert *et al.* 1977). There is controversy about the history of these systems and the presumably related formation of the central galaxy. Ostriker & Tremaine (1975) suggest that a cD galaxy grows by accreting other galaxies through dynamical friction and tidal stripping; Merritt (1985) suggests that galaxies merge during the original cluster collapse. Recent *N*-body simulations by Bode *et al.* (1994) and Dubinski (1997) produce giant central elliptical galaxies through hierarchical merging. Fabian (1994) proposes that enhanced star formation at the cluster center resulting from a cooling flow may further enlarge these merged galaxies.

The AWM/MKW clusters span a broad range of velocity dispersions ($\sigma \sim 100 - 700$ km s $^{-1}$) and more than two orders of magnitude in X-ray luminosity (Beers *et al.* 1995, Kriss *et al.* 1980, 1983). Detailed study of these systems may thus discriminate among these scenarios. These systems are dynamically fairly simple in their centers, without much substructure in the central $1h^{-1}$ Mpc, although there is evidence for complexity on larger scales (Beers *et al.* 1995). They are sufficiently nearby that a complete sample can be analyzed to reasonable limiting magnitude with modest instrumentation. X-ray data in conjunction with optical studies provide a foundation for equilibrium mass models of these clusters.

Early optical studies of AWM/MKW systems lack extensive photometry and complete redshift samples (Beers *et al.* 1984, 1995 and references therein; Malumuth & Kriss 1986; Williams & Lynch 1991, Price *et al.* 1991; Dell'Antonio *et al.* 1995). AWM 7 is particularly problematic because it spans two Palomar Sky Survey plates with rather different sensitivities, making consistent photographic magnitude determination difficult. Previous optical determinations of the mass-to-light ratio of AWM 7 (Kriss *et al.* 1983, Beers *et al.* 1984) yield values exceeding $1000 h M_\odot/L_\odot$, a result exacerbated by the cluster's high velocity dispersion. The optical data are discrepant with X-ray determinations in the range $200-500 h M_\odot/L_\odot$ (Dell'Antonio *et al.* 1995, Neumann & Böhringer 1995). Our new complete photometric and spectroscopic data yield $\sim 650 \pm 150 h M_\odot/L_\odot$, consistent with the range for other clusters and with the X-ray data for AWM 7. Optical mass-to-light determinations for other AWM/MKW systems by Beers *et al.* (1995) are generally consistent with X-ray results.

AWM 7 is the first system in our study of a complete sample of nearby AWM/MKW clusters. It is one of the nearest clusters (~ 5200 km s $^{-1}$) and is the one with the largest velocity dispersion (~ 700 km s $^{-1}$). We have measured 172 magnitudes and redshifts in AWM 7, making it one of the best-sampled systems in the sky.

In §2, we discuss the data acquisition and reduction, and define the cluster sample. In §3, we discuss the cluster kinematics and segregation by spectral type, search for substructure, and examine the velocity dispersion profile. In §4, we discuss the photometric properties, compute the luminosity function of the cluster, and compute the mass-to-light ratio. We discuss the ramifications in §5 and conclude in §6.

2. Observations

AWM 7 is a poor cluster with the cD galaxy NGC 1129 ($\alpha = 2:54:27$, $\delta = 41:34:47$ J2000) at its center. The recession velocity of the cD is 5288 ± 71 km s $^{-1}$. The cluster has a mean radial velocity 5247 ± 76 km s $^{-1}$. Here we describe our observations of the system, and define the cluster sample.

We measured redshifts of 172 galaxies within a projected distance of $1.6 h^{-1}$ Mpc from NGC 1129, and obtained R -band CCD photometry for the central $1.15 \times 1.15 h^{-1}$ Mpc of the cluster. 127 of the galaxies with redshifts are in the region with CCD photometry.

Table 1 contains the velocities and R -band magnitudes for the 172 galaxies. Column 1 lists the galaxy RA; column 2, the declination; column 3, the radial velocity; column 4, the uncertainty in the radial velocity; column 5, the isophotal magnitude (to 23.5 mag asec $^{-2}$ in R_{KC}); column 6, the error in isophotal magnitude; column 7, the source of the magnitude (CCD or POSS); column 8, the spectral type (presence or absence of H α emission, quantified in §3); and column 9, the extinction A_R along the line of sight to the galaxy.

2.1. Redshifts

We measured 140 redshifts with the FAST spectrograph on the Whipple Observatory 1.5-m Tillinghast telescope in Nov.–Dec. 1995 and a further 43 with the MMT Blue Channel Spectrograph on 1996 Dec. 5–6; yielding 172 galaxy redshifts. To ensure uniform spectroscopy with a well-understood error model, we obtained a new spectrum for each galaxy despite some previous measurements in the literature (*e.g.* Beers *et al.* 1995 and references therein). Kurtz & Mink (1998) discuss in detail how FAST velocities compare to other measurements; briefly, the instrumental velocity offset with respect to the night sky is less than 10 km s $^{-1}$ and is indistinguishable from zero. The FAST spectra have 6 Å resolution and spectral coverage of 3600–7600 Å. The MMT spectra have 10.6 Å resolution and coverage of 3000–8000 Å. We reduced the spectra by cross-correlation, using the IRAF

XCSAO task (Kurtz & Mink 1998).

Most galaxies in our survey are absorption-line systems. For these, the mean uncertainty in the measured velocities is ~ 35 km s $^{-1}$. For the emission-line galaxies we add an extra error term of 60 km s $^{-1}$ in quadrature because the line-emitting regions do not necessarily trace the galaxy center of mass (Kurtz & Mink 1998); the values tabulated in Table 1 incorporate this extra term.

We used the Digitized Palomar Observatory Sky Survey scans to select targets for observation with FAST within a $2^\circ \times 2^\circ$ region centered on NGC 1129. AWM 7 spans two POSS plates that differ greatly in sensitivity. Uniform magnitude determinations are thus difficult; the problem is compounded by vignetting at the plate edges. On the basis of the CCD photometry we later defined a sample complete to $R = 16.5$ covering the central $75' \times 75'$ ($1.15 \times 1.15 h^{-1}$ Mpc). We used the MMT to measure redshifts of galaxies with $R \gtrsim 16.0$.

2.2. Photometry

We acquired an R -band mosaic of the central $75' \times 75'$ of the cluster with the MDM 1.3-m telescope during Nov. 1995. There are 36 six-minute $13.7' \times 13.7'$ exposures, with $1.2'$ overlap between frames. Conditions were photometric for most of the images; we correct the 4 non-photometric images using the overlap regions with neighboring photometric frames. The rms error in the photometric solutions are 0.0196 and 0.0370 mag for the two photometric nights. We determine isophotal magnitudes with the FOCAS package. The quoted magnitudes are isophotal to $R = 23.5$ mag/arcsec 2 , which is more than 2σ above the sky noise in each frame. We reviewed the star/galaxy separation manually for all non-stellar objects brighter than $R_{23.5} = 18.5$ to remove misclassified objects — FOCAS tends to misclassify double stars as galaxies.

FOCAS magnitudes are sensitive to the local sky. FOCAS is optimized for faint objects, and tends to underestimate the luminosity of bright extended objects systematically, assigning much of the diffuse light to the sky rather than to the object. Moreover, because the isophotes are defined by the number of σ in excess of sky, the determination of the sky σ in each frame is critical. There are flaws in the FOCAS software which lead to systematic errors in the sky determination. The presence of bright stars at the bottom edge of an image results in comet-like swaths of spuriously bright sky extending up the image. Blocking out the stars by hand removes this effect, but its very existence adds uncertainty to the sky determination, and hence to the isophotal magnitudes. We thus add 0.05 mag

in quadrature to the magnitude errors, derived otherwise from the rms scatter in the photometric solution; for the non-photometric images, we also include the uncertainty in the zeropoint as determined from the rms magnitude error for isolated stars in the overlap regions. We quote an error of 0.25 mag for the Digitized POSS magnitudes (Geller *et al.* 1997), although the scatter is in fact likely greater for AWM 7 because of the different sensitivities of the two plates spanned by the cluster.

We use galaxies in overlap regions of the mosaic to check the consistency of the magnitudes; in Fig. 1 we plot the difference in the magnitude measurements for individual galaxies as determined from different mosaic fields. We plot the differences as a function of the brighter magnitude. When a galaxy appears in more than two fields, we plot the greatest difference against the brightest magnitude. The mean difference is 0.043 mag, with a scatter of 0.036 mag.

We calculate an extinction correction for each galaxy from the relation $A_R = 2.5E(B - V)$ (Zombeck 1992), with the color related to the HI column density by $\langle N(\text{HI})/E(B - V) \rangle = 4.8 \times 10^{21} \text{ atoms cm}^{-2} \text{ mag}^{-1}$ (Bohlin *et al.* 1978). We obtain the HI column density along the line of sight to each galaxy from the Bell Labs HI maps (Stark *et al.* 1992). The extinction in the total sample of 172 galaxies ranges from 0.40 to 0.54 mag; the gradient arises from the cluster’s proximity to the galactic plane ($b_{\text{cD}} = -15^\circ 6$). Within the region with CCD photometry, the extinction ranges from 0.42 to 0.50. These values exceed those on the map of Burstein & Heiles (1982) by ~ 0.15 mag. The magnitudes listed in Table 1 are the measured magnitudes, uncorrected for the extinction in column (9). Calculations of the luminosity function below do account for the extinction.

2.3. Defining the cluster sample

Figure 2a shows the redshift distribution for all 172 galaxies; large-scale structure is apparent behind the cluster at $\sim 20000 \text{ km s}^{-1}$, and more weakly at $\sim 10000 \text{ km s}^{-1}$. In the range 2500 – 7500 km s^{-1} there are 106 galaxies, which we identify as cluster members; we denote this set of galaxies the “C” sample. The line under the histogram in Figure 2b indicates this range and the dotted line indicates the redshift of the central cD galaxy ($5288 \pm 71 \text{ km s}^{-1}$). For these 106 galaxies, $c\bar{z} = 5247 \pm 76 \text{ km s}^{-1}$ and $\sigma = 783_{-49}^{+60} \text{ km s}^{-1}$ (Danese *et al.* 1980, 68% confidence). There is a 779 km s^{-1} velocity gap between the highest-redshift cluster galaxy and the lowest-redshift background galaxy; this is a $\sim 1\sigma$ gap starting 2.5σ above the cluster mean. There is no obvious foreground.

82 of the 106 C galaxies lie within the region with CCD photometry; Figure 2c shows

their velocity distribution. This sample is 100% complete to $R = 16.3$, 99% complete to $R = 16.5$, 98% complete to $R = 16.7$, and 96% complete to $R = 16.9$ (uncorrected magnitudes); for this subsample, $c\bar{z} = 5248 \pm 82$ km s $^{-1}$ and $\sigma = 747_{-52}^{+66}$ km s $^{-1}$, clearly consistent with the larger sample. We denote this set of galaxies the “ML” sample.

There are 134 galaxies in the central $75' \times 75'$ (1.56 deg 2) with $R_{23.5} \leq 17$, of which 122 have measured redshifts; of these, the 82 ML galaxies have velocities in the range 2500–7500 km s $^{-1}$. Assuming that 82/122 of the 12 unmeasured galaxies also lie in the cluster, we estimate that there are 4 ± 2 additional background galaxies, for a total of 44 ± 5 , or 28 ± 3 per square degree. Representing the background count by

$$n_b = C_0 \int_{-\infty}^{m_{\text{lim}}} 10^{d_0 m} dm \text{ deg}^{-2}$$

and using values of d_0 and C_0 derived from the Century Survey (Geller *et al.* 1997) yields $n_b = 36 \pm 6$ deg $^{-2}$ for $m_{\text{lim}} = 16.9$, consistent with the background we observe. The quoted errors are Poisson errors, which underestimate the true error due to clustering.

We investigate the peak in the velocity histogram (Fig. 2a) at $\sim 18,000$ km s $^{-1}$. We plot the spatial distribution of the background galaxies in Fig. 3; the non-uniform distribution of the background galaxies adds some uncertainty to the computation of the faint end of the LF (§4.3) and to the background-subtraction statistics.

3. Kinematics

We use the C sample to examine the kinematics of the cluster. This sample is magnitude-limited only within the area of the CCD survey. We separate our sample by spectral type (presence/absence of H α); the two subsamples have quite different kinematics. We test for substructure in the cluster and examine the cluster velocity dispersion profile as a function of radius.

3.1. Velocity Histogram

The velocity distribution in Figure 2b appears bimodal with an apparent peak near 4500 km s $^{-1}$. However, a Kolmogorov-Smirnov test (Press *et al.* 1992) shows that the distribution is consistent with a Gaussian velocity distribution of mean 5247 km s $^{-1}$ and dispersion 783 km s $^{-1}$ ($P_{D>D_{\text{obs}}} = 0.73$).

3.2. Spectral Segregation

We separate the sample into emission (Em) and non-emission (Ab) galaxies, based on the presence or absence of $\text{H}\alpha$ emission in the spectrum. We use two criteria for including a galaxy in the Em sample. The first is that the redshift derived from cross-correlating against the emission-line template lie within 200 km s^{-1} of the redshift derived from the best-fit template; if the emission-line template fits best, this criterion is automatically satisfied. The second criterion is that the EMSAO task in the IRAF RVSAO package must detect and correctly identify $\text{H}\alpha$ given the best-fit redshift. If both criteria are satisfied, we classify the galaxy as Em; if neither, as Ab. If the first criterion is satisfied and not the second, the galaxy is classified as Ab; given the correct redshift, EMSAO would identify any strong $\text{H}\alpha$ that were present. If the second criterion is satisfied but not the first, we inspect the spectra visually; most such galaxies are ultimately classified as Em. The robustness of the classification is clearly a function of the signal-to-noise ratio of the spectrum; emission line galaxies with poor signal-to-noise or only weak emission may be misclassified as non-emission if the $\text{H}\alpha$ emission line does not rise appreciably above the noise. For Em galaxies with strong emission lines and high S/N spectra, the emission-line $\text{H}\alpha$ equivalent widths are typically $\gtrsim 7 \text{ \AA}$; these are indicated with an asterisk in Table 1. The equivalent widths in the other Em galaxies (those with intrinsically weaker lines, or just with lower S/N spectra) range from 2 to 7 \AA . Of the 172 galaxies observed, 50 show emission and 122 do not; of the 82 galaxies in the ML sample, only 9 show $\text{H}\alpha$ emission.

The Em and Ab galaxies are spatially segregated. Fig. 4 shows the distribution of 106 galaxies for which $2500 \text{ km s}^{-1} < cz < 7500 \text{ km s}^{-1}$, with emission-line galaxies plotted as circles and non-emission galaxies as crosses. The distribution of emission-line galaxies is not centrally concentrated, nor is it centered on the cD. The median distance of the Em galaxies from the central cD galaxy is $44.6'$; for the Ab galaxies it is $17.8'$.

The velocity and magnitude distributions of the emission-line and non-emission galaxies also differ. Fig. 5 shows the velocity distribution of the Em and Ab galaxies separately for the ML sample in the upper panel, and for all observed galaxies in the lower panel. The 9 emission-line galaxies have $c\bar{z} = 4971 \pm 438 \text{ km s}^{-1}$, $\sigma = 1313^{+503}_{-233} \text{ km s}^{-1}$; the 73 non-emission galaxies have $c\bar{z} = 5304 \pm 75 \text{ km s}^{-1}$, $\sigma = 643^{+61}_{-48} \text{ km s}^{-1}$. The velocity distribution of the Em galaxies is apparently much broader, but because of the small size of the sample, a two-sample K-S test rules out the Em and Ab galaxies' being drawn from the same underlying velocity distribution with only 97% confidence.

Figure 6 shows velocity as a function of angular distance from the cluster for all 106 C galaxies. The greater central concentration of the Ab galaxies is apparent, as is their smaller velocity dispersion. Moreover, all but one of the 13 faint ($R > 16.3$) cluster galaxies

are absorption line systems. We discuss the magnitude distribution in more detail in §4.

The cluster Abell 576 shows similar behavior (Mohr *et al.* 1996a); there too the Em galaxies are less spatially concentrated, have a greater velocity dispersion, and are systematically fainter than the Ab galaxies, but they are not offset from the cluster center. The core velocity dispersions of the Ab galaxies are ~ 530 km s $^{-1}$ in both AWM 7 and A 576, but the velocity dispersion profile rises more steeply and to a higher value in A 576; at 1 Mpc, $\sigma_{\text{A}576} \sim 1000$ km s $^{-1}$. The ratio of Em to Ab galaxies is larger in A 576 (79:142). We follow the procedure adopted by Mohr *et al.* (1996a) and consider the Em and Ab samples separately below. We base our estimates of the mass-to-light ratio on the Ab galaxies only.

3.3. Substructure

We use the Dressler-Shectman statistic (Dressler & Shectman 1988) to test for substructure in the cluster. They define the statistic $\Delta_0 = \sum_i \delta_i$, where the summation is over all galaxies and

$$\delta_i \equiv \frac{n}{\sigma_g^2} [(\bar{v}_g - \bar{v}_i)^2 + (\sigma_g - \sigma_i)^2]^{1/2}$$

is a measure of the deviation of the local mean velocity and dispersion (\bar{v}_i , σ_i) from the global cluster values (\bar{v}_g , σ_g). For each galaxy, δ_i is a function of the number of nearest neighbors n entering into the calculation of the local \bar{v}_i and σ_i . We evaluate the significance of Δ_0 for each n by randomly shuffling the velocities of all galaxies 5000 times, and re-calculating Δ_0 each time. We thus obtain a distribution of Δ_0 against which to compare the actual value.

A D-S test with $n = 11$ indicates that there is substructure in the northwest of the cluster, where the Em galaxies predominate. Because the Δ_0 statistic characterizes local deviations of the mean and dispersion from the overall cluster values, this substructure reflects the larger dispersion of the Em galaxies seen in Fig. 5. The significance of the substructure detection is marginal. Figure 7 shows the D-S statistic for the 106 C galaxies as a function of subgroup size n for $5 \leq n \leq 90$ in the top panel, with the probability of an equal or greater D-S statistic arising by chance (determined from the 5000 Monte Carlo simulations for each n) in the lower panel. A low P_{false} indicates a high significance for the substructure detection. The substructure is most significant for $n = 13$, but even then there is still a greater than 2% chance of an equal or greater Δ_0 arising by chance. When we exclude the Em galaxies and perform the D-S test on the remaining 88 Ab galaxies, there is no discernible substructure for any value of n (not shown); the distribution of Ab

galaxies is smooth. This analysis supports the idea that the Em galaxies are a dynamically distinct population of late-type galaxies; our sample does not contain enough Em galaxies to determine their large-scale dynamics. It may be that, as in A 576, they are infalling.

3.4. Velocity Dispersion Profile

Figure 8 plots the velocity dispersion of the 88 non-emission C galaxies as a function of cluster radius. We take the cD as the geometric center of the cluster; Neumann & Böhringer (1995, hereafter NB) find that the cD coincides exactly with the maximum of the X-ray emission. The plot extends to 2200 arcsec, the radius to which our photometric and kinematic data are both complete.

Each point in the upper panel of Fig. 8 represents the velocity dispersion of 11 galaxies ranked sequentially in distance from the cD; neighboring points are thus correlated, but represent annuli of different widths. Uncorrelated points are distinguished by 68% confidence-level error bars. The lower panels plot the velocity and magnitude of the galaxies along with a moving median curve; uncorrelated points are indicated by filled boxes along the curve. The data point for NGC 1129 is a measurement of its internal velocity dispersion from Malumuth & Kirshner (1985), with a $4'' \times 10''$ aperture. The internal $\sigma = 335 \pm 25$ km s^{-1} is substantially less than the velocity dispersion in the cluster core.

The median velocity throughout the core strays little from the overall cluster median; However, the cluster velocity dispersion appears lower in the core. Within $0.1h^{-1}$ Mpc of the center, $\sigma \sim 550_{-100}^{+150}$ km s^{-1} , some 200 km s^{-1} lower than at the periphery; about 20 galaxies comprise the cold core. To assess the significance of the cold core, we split the sample by radius and evaluate σ separately for galaxies within and external to the delimiting radius. This analysis indicates that the core is cooler than the outskirts, but only at the $\sim 1\sigma$ level. The evidence for a cold core from $\sigma(r)$ alone is thus present, but weak. The scale of the cold core matches the scale of the X-ray cooling flow seen by NB.

Diaferio (1997) proposes a simple dynamical explanation for a cold core. Under the assumption of virial equilibrium (probably valid for the Ab-type galaxies in the core),

$$\sigma^2 \propto \frac{GM(< r)}{r} .$$

Representing the radial mass density profile by a power law $\rho(r) \propto r^{-\alpha}$ yields

$$M(< r) \propto \int_0^r \rho(x)x^2 dx \propto r^{3-\alpha} ,$$

so $\sigma \propto r^{1-\alpha/2}$. Thus $\alpha < 2$ results in a rising $\sigma(r)$ profile, and $\alpha > 2$ in a falling profile. The mass model of Navarro *et al.* (1995) posits $\rho(r) \propto r^{-1}(r + r_s)^{-2}$, which behaves as r^{-1} for small r , giving $\sigma(r) \propto r^{1/2}$, a rising profile. Alternatively, the common β -model (Cavaliere & Fusco-Femiano 1978) has $\rho(r) \propto [1 + (r/r_c)^2]^{-3\beta/2}$, implying constant density for $r \ll r_c$, and so $\sigma(r) \propto r$ in this regime. NB find $r_c = 51 \pm 3h^{-1}$ kpc for AWM 7. Thus the r -dependence of σ in the core ($r < r_c$) would only be detectable with very dense sampling of the cluster core to overcome small-number Poisson statistics, the sensitivity of σ to outliers, and the small angular extent of the core. Our sampling is too sparse to characterize any rise within r_c as more representative of one model density profile or the other; a deeper sample could in principle discriminate between them. However, the cluster core has relatively few faint galaxies, and the core sampling may never be dense enough to discriminate.

4. Photometric Properties

Figure 9 shows the differential and cumulative magnitude distribution of the 82 ML galaxies, with the Em galaxies alone as the dotted histogram. Here we correct the magnitudes for extinction. At the mean sample redshift of 5247 km s^{-1} , $m = M + 33.60 - 5 \log h$. A fiducial absolute magnitude for the field $M_{*F} = -20.7$ in the R -band from the Century Survey (Geller *et al.* 1997) yields a corresponding $m_{*F} = 13.35 - 5 \log h$. AWM 7 contains three galaxies substantially brighter than m_{*F} , and seven of comparable magnitude.

The distribution of the Em galaxies is flat as a function of magnitude; significantly, only one galaxy fainter than 16.3 is an emission-line galaxy. The median magnitude of the Em sample is $R = 15.44$; the median of the Ab sample is $R = 14.67$. The offset between the magnitude distributions probably reflects the $\Delta(B - R) \sim 1$ mag color difference between late- and early-type galaxies. At B , the Em and Ab galaxies would have more concordant magnitude distributions, consistent with field measurements (Marzke *et al.* 1994). A similar offset between the spectral types is seen in A 576.

4.1. Surface Brightness

Figure 10 shows the mean and core surface brightness for the 82 sample galaxies. The core surface brightness is determined in the most luminous 3×3 pixel grid in the object, corresponding to an area $1''.33$ square on the sky; we compute the mean surface brightness within the $R = 23.5$ isophote. We plot Em galaxies as triangles and Ab galaxies as squares.

There is a clear trend of decreasing surface brightness with increasing magnitude. This trend makes the observation of fainter objects more difficult, and leads to some undercounting of faint sources, artificially depressing the faint end of the luminosity function.

The brightest galaxy (the cD N1129) is anomalous. A cD galaxy is a giant elliptical with an extended low surface brightness envelope (Oemler 1976). This envelope lowers the mean surface brightness within the $R = 23.5$ isophote for NGC 1129, since it occupies a large fraction of the area within the limiting isophote. The distended envelope also makes the isophotal magnitude more sensitive to the sky subtraction because the brightness profile approaches the sky level more gradually.

4.2. Magnitude Segregation

Magnitude (or equivalently luminosity) segregation is usually interpreted as an indicator of mass segregation; the more massive (and hence more luminous) galaxies are more centrally concentrated and move more slowly than less massive (luminous) ones. den Hartog & Katgert (1996) find luminosity segregation in 25 of their sample of 71 clusters, with a strong signal in 10.

The central panel of Fig. 8 shows m_R as a function of cluster radius in AWM 7, with a moving 11-galaxy average superimposed. The median magnitude of galaxies within $r \lesssim 0.1h^{-1}$ Mpc is brighter than the median outside this radius, although the significance is low because of the small sample size. The radial extent of this luminosity excess is roughly coincident (within a factor of 2) with NB’s value of $r_c = 51 \pm 3$ kpc for the X-ray core. The extent of the excess also matches the region of reduced velocity dispersion, suggesting that the cold X-ray core, the reduced velocity dispersion, and the luminosity excess are related physical effects.

4.3. Luminosity Function

The most striking feature of the luminosity function (LF) of AWM 7 (Fig. 9) is the peak near $R \sim 13.7$ and the subsequent dip in galaxy counts near $m_R \sim 14.5$ ($M_R \sim -19.1$). The cumulative distribution shows that although the peak is enhanced by the binning, the dip is not an artifact. A similar feature appears in the Coma cluster (Bernstein *et al.* 1995, Biviano *et al.* 1995), in three of four moderate-redshift Abell clusters studied by Wilson *et al.* (1997), and in a sample of 20 Abell clusters studied by Gaidos (1997). Biviano *et al.* determine Coma cluster membership spectroscopically (unlike Bernstein *et al.*, Wilson *et*

al., and Gaidos, who do so statistically), and suggest that this feature may be common to rich clusters.

We attempt to characterize the cluster LF in terms of the Schechter (1976) function parameters α (logarithmic faint-end slope) and M_* (characteristic luminosity). Measured values of α in clusters range from -1.0 (Lopez-Cruz *et al.* 1997, Gaidos 1997) to -2.2 in B and I (De Propris *et al.* 1995); the inclusion of dwarf galaxies and low surface brightness galaxies increases the faint-end slope (López-Cruz *et al.* 1997, Sprayberry *et al.* 1997). In the case of Coma, the inclusion of dwarf galaxies boosts the estimate of α from -1.35 to -1.7 (Trentham 1997). Trentham (1997) argues that since only dSph galaxies obey a power-law distribution, the faint-end slope of the LF is a misleading indicator, dominated primarily by its coupling to M_* . He notes that other galaxy types have bounded LFs, yet it is precisely these other types that enter into most cluster LF determinations.

The Schechter function describes the LF of AWM 7 poorly; it cannot accommodate the peak and subsequent dip in the distribution. Maximum-likelihood fitting (Efstathiou *et al.* 1991) of a Schechter function to the magnitude distribution (not shown) forces M_* to the peak near $R \sim 14$ and results in an ill-fitting declining faint end, in contrast to the increasing counts seen in the last three complete bins of the actual distribution. Therefore, we obtain an estimate of the faint-end slope of the LF by extrapolation. We subtract a background field galaxy count, given by $n(m) \propto 10^{0.6m} dm \deg^{-2}$ and normalized to the Century Survey, from the observed galaxy counts (with or without measured redshifts) to $R = 17.5$ (corrected for extinction), and fit a power law to the residual in the range $15.0 < R < 17.5$. We plot the result in Fig. 11. The upper magnitude limit of the fit is set by the incompleteness of the galaxy counts at faint magnitudes due to poor star-galaxy separation on the CCD images with bad seeing. The best-fit power law corresponds to a Schechter parameter $\alpha = -1.37 \pm 0.16$, with formal $\chi^2/\nu = 3.57/6$.

We conclude that like Coma, AWM 7 has a LF with a bump at the bright end and a steep faint end. The steep faint end seen in field galaxy surveys (*e.g.* Marzke *et al.* 1994, Marzke & da Costa 1997) is due to blue galaxies. In AWM 7, the LF is steep and red, populated by absorption-line systems. Mobasher & Trentham (1998) find that the steep ($\alpha \sim -1.4$) K -band LF in Coma is due to dwarf spheroidals. The issue is complicated by surface-brightness selection effects: low-surface-brightness galaxies may be missing from field surveys, which consequently underestimate their contribution to the faint-end slope.

4.4. Mass-to-Light Ratio

Owing to the absence of precise photometry over a large area, the mass-to-light ratio of AWM 7 has been poorly known. Estimates have ranged from $160 h$ in V (in units of M_\odot/L_\odot) (Kriss *et al.* 1983, based on Einstein IPC data) to $1120 h$ in B (Beers *et al.* 1984, virial mass estimator). Using ROSAT data, Dell’Antonio *et al.* (1995) find a value of $440 h$ in B , and NB constrain the ratio to the range $400\text{--}1100 h$ in B . Kriss *et al.* (1983) find a range $140\text{--}200 h$ in V for four other MKW and AWM groups. The main uncertainty in X-ray determinations of the mass is introduced by the cooling flow.

We compute the mass from the virial estimator appropriate for the case of galaxies embedded in a diffuse distribution of dark matter, with the added assumption that the galaxies trace the dark matter distribution. We exclude the Em galaxies from the computations on the grounds that they constitute a dynamically distinct population superposed on the virialized, Ab-populated cluster. The appropriate estimator (Binney & Tremaine 1987) is

$$M_{\text{est}} = \frac{3\pi N}{2G} \frac{\sum_{i=1}^N v_i^2}{\sum_{i=1}^N \sum_{j < i} |R_i - R_j|^{-1}}$$

where v_i is the radial velocity relative to the cluster mean, and R_i is the projected distance from the cluster center. This estimator assumes that the galaxies are in dynamical equilibrium within the cluster potential, and that the galaxies trace the total mass. If the dark matter is more extended than the galaxy distribution, this prescription underestimates the M/L ratio. This mass estimate is also very sensitive to the inclusion of foreground or background galaxies. We estimate the error in the mass profile by the statistical “jackknife” procedure (Diaconis & Efron 1983) as follows: within each projected radius, we calculate the mass independently for all n subsets of $n - 1$ galaxies, where n is the total number of galaxies within said radius, and with the velocities shuffled randomly for each subset. We define the standard deviation about the mean of the n masses thus computed to be the error in the mass estimate within that projected radius.

In principle this mass estimate should be adjusted by a surface term (The & White 1986) because the entire system is not included in the observed sample. Inclusion of this term requires knowledge of $\sigma(r)$, $N(r)$, and the dark matter profile. The first two factors can be constrained from the data, and the dark matter profile can be reasonably described by model fits to hierarchical clustering simulations as in Navarro *et al.* (1997). However, our data set is not extensive enough to support this analysis robustly; we do not have broad enough angular coverage to self-consistently compute the core radius. We have calculated the surface term, and find that the error is comparable to the value of the correction itself. Thus the masses we quote below do *not* incorporate a surface term.

The top panel of Figure 12 shows our integrated mass profile, computed by applying the virial mass estimator to successively larger radii, along with the profile determined by NB from a ROSAT temperature profile and a data point from dell’Antonio *et al.* (1995). The mass enclosed within $0.25 h^{-1}$ Mpc is $\sim 9 \times 10^{13} M_\odot$, rising to $\sim 2 \times 10^{14} M_\odot$ within $0.6 h^{-1}$ Mpc. Our profile is in good agreement with the value derived by Dell’Antonio *et al.* (1995) from X-ray data, who estimate $8 \times 10^{13} h^{-1} M_\odot$ within $0.25 h^{-1}$ Mpc; it also lies within the errors of the NB profile for radii up to $\sim 0.5 h^{-1}$ Mpc. Beyond this radius, their mass estimates exceed ours; Fig. 12 shows their profile diverging from ours increasingly at large radii. They derive the mass profile beyond $\sim 600 h^{-1}$ Mpc by extrapolation, however, and their luminosity, taken from Beers *et al.* (1984), is an underestimate which increases the computed M/L ratio.

We compute the R -band light by adding up the luminosities of the galaxies in our sample and correcting for incompleteness. The correction is required because for any magnitude-limited sample, the observed luminosity is necessarily an underestimate of the total cluster luminosity because the faintest galaxies are not observed. We correct for this incompleteness by integrating the extrapolated luminosity function out to infinite magnitude. For a Schechter function, the observed fraction of the total luminosity is given by $\Gamma(\alpha + 2, L_{\min}/L_*)/\Gamma(\alpha + 2)$, where L_{\min} and L_* are the luminosities corresponding to the completeness limit and M_* , respectively, and $\Gamma(x, y)$ is the incomplete gamma function. The completeness limit $R = 16.5$ is 3.6 mag fainter than $M_* = -20.7$, yielding an observed luminosity fraction of $\sim 90\%$. A 0.5 mag error in the completeness limit corresponds to a 5% error in the observed luminosity fraction in this regime. We observe $2.6 \times 10^{11} L_\odot$ in the R -band within a projected radius of $0.6 h^{-1}$ Mpc, yielding a corrected total luminosity of $2.9 \times 10^{11} L_\odot$. The cD alone contributes $\sim 14\%$ of the R -band luminosity within this radius.

We plot the M/L profile in the lower panel of Fig. 12. The data point for NGC 1129 is from Bacon *et al.* (1985), who tabulate mass-to-light ratios for 197 ellipticals. The mean M/L_B in their sample is 13; NGC 1129’s ratio of $M/L_B = 94 \pm 31$ is the largest in their sample. We derive a M/L_R ratio of $\sim 600 h M_\odot/L_{\odot, R}$ for the cluster that remains fairly constant outside a projected radius of $0.3 h^{-1}$ Mpc, rising to $\sim 650 \pm 170 h M_\odot/L_{\odot, R}$ near $0.45 h^{-1}$ Mpc. We include only the errors on the mass. For comparison, note that $M/L_B = 1.58 M/L_R$ because $(B - R)_\odot = 1.0$, but for elliptical galaxies typically $B - R = 1.5$. Our value of the mass-to-light ratio is at the low end of the range of NB, where values are based on extrapolations of X-ray temperature profiles to 1° . Within $0.25 h^{-1}$ Mpc, Dell’Antonio *et al.* report $430 h$ in the B -band, corresponding to $272 h$ in R ; we find $530 h$. Given the agreement in mass, the discrepancy arises from differences in luminosity; Dell’Antonio *et al.* (1994) do not directly measure the luminosity in the

cluster but instead determine cluster membership by background subtraction, and then calibrate magnitudes derived from POSS plate scans against Zwicky (1962) magnitudes, whose scatter is ~ 0.3 mag (Bothun & Cornell 1990, Geller *et al.* 1997). Their largest source of error is the plate photometry, particularly in light of the considerable variation of the photographic sensitivity across the cluster, which introduces a large systematic error in addition to the intrinsic scatter in the calibration magnitudes.

The mass-to-light ratio of AWM 7 is lower in the center than at the periphery, because the depressed central velocity dispersion lowers the mass estimate, and because there is excess luminosity in the core. It is interesting to note that the M/L profile at small radii approaches the value for the cD. The profile also flattens outside $\sim 0.3 h^{-1}$ Mpc, rising only another 10% out to $0.6 h^{-1}$ Mpc, suggesting that the dark matter is less concentrated than the light. The mass-to-light ratio levels off at roughly twice the projected radius at which the velocity dispersion does.

Our calculated mass-to-light ratio for AWM 7 is in close agreement with the values determined by Mohr *et al.* (1996b) for the clusters A 2626 and A 2440: they find $M/L_R \sim 610 h$ and $660 - 880 h$, respectively, from a joint X-ray and optical study of the clusters. Carlberg *et al.* (1996, 1997) overlay 14 clusters to form an aggregate whose M/L ratio they find to be $289 \pm 50 h (M/L)_\odot$ in Gunn r . Cirimele *et al.* (1997) overlay 12 Abell clusters and find M/L_V in the range 140–440 h . Measurements of M/L ratios for distant clusters using weak lensing yield a similar range of values: Tyson & Fischer (1995) find $M/L_V = 400 \pm 60 h (M/L)_\odot$ for A 1689 at $z = 0.18$, while Carlberg *et al.* (1994) report 225 h in the V -band for a cluster at $z = 0.325$, and 275 h for Coma, corrected for “modest” evolution of the galaxy LF. In this context, AWM 7 no longer appears so exceptional.

5. Discussion

Our optical and spectroscopic survey of the central $1.2 \times 1.2 h^{-1}$ Mpc of AWM 7 yields a velocity dispersion profile, mass profile, luminosity function, and mass-to-light profile of the cluster. There is three-fold evidence for a cold core in the cluster: the central velocity dispersion is depressed, there is luminosity segregation on the same scale, with excess luminosity in the core, and there is a cold X-ray core with similar scale. The optically-determined mass is in good agreement with X-ray determinations by NB and by Dell’Antonio *et al.* (1995). Despite the offset in X-ray isophotes they see, we find no kinematic evidence for substructure. The luminosity function of AWM 7 is peculiar: there is a dearth of galaxies with $R \sim 14.5$, an excess of galaxies just brighter, and a steeply rising faint end. The faint end is populated almost exclusively by red, absorption-line galaxies,

in contrast to the blue mIrr which dominate the steep faint end in the field Marzke *et al.* (1994).

5.1. Evolution of the Luminosity Function and Formation of the cD

The formation of cD galaxies is closely tied to questions of LF evolution, universality, and mass segregation. Theories for cD formation include merging of dwarf galaxies through dynamical friction (Ostriker & Tremaine 1975; White 1976; Ostriker & Hausmann 1977), cannibalization of neighboring galaxies (Gallagher & Ostriker 1972; Richstone 1975, 1976), primordial origin (Merritt 1984), and mergers of large, bright galaxies early in the cluster history, with additional growth from accumulation of tidal debris or from cooling flows (Fabian & Nulsen 1977; Cowie & Binney 1977; Fabian *et al.* 1984).

Active merging in a cluster would result in substantial evolution of the LF. Thus the LF could in principle be used as an estimator of the dynamical age of the cluster. Although the traditional “cannibalization” merger scenarios held that dwarf galaxies agglomerate into larger ellipticals (see Barnes & Hernquist 1992a for a review), recent simulations (Barnes 1992, Dubinski 1997) indicate that larger galaxies tend to merge, with an abundance of faint galaxies condensing from the tidal tails produced in these interactions (Barnes & Hernquist 1992b). This scenario can explain many features of the LF: the dip may reflect depletion of galaxies through merging; the peak brightward of the dip has a dynamical origin — it is populated by products of these mergers; and the steep faint end arises from the dwarfs formed from the tidal tails of the mergers.

Early theories that mergers deplete the dwarf population should result in a paucity of red dwarfs, particularly in clusters with low velocity dispersion where mergers are more efficient (David & Blumenthal 1992). High-dispersion clusters may have lower merger rates and thus more red dwarfs at the current epoch. In this paradigm, AWM 7’s high velocity dispersion would suppress merging and would thus account for the steep, red faint end, but could not explain the other features of the LF, including the bump and the presence of the cD.

AWM 7 presents a steep, red dwarf population in a high-dispersion cluster, which argues against the merger of pre-existing dwarfs as the source of the cD, both because (1) mergers are *a priori* unlikely due to the high σ , and (2) mergers of dwarfs to form the cD would deplete the faint end. Unless AWM 7 initially had an even steeper faint end, this scenario seems unlikely.

6. Conclusion

Our study of AWM 7 reveals two important features: the cluster has a cold core, and the steeply rising faint end of the LF is populated predominantly by absorption-line galaxies, in contrast to the emission-line galaxies that populate the faint end of the field LF. In AWM 7, the emission galaxies are probably a dynamically distinct infalling population superposed on the relaxed system of absorption-line galaxies; the little substructure that is apparent in the velocity data is entirely attributable to the emission galaxies. We have resolved the anomalous earlier mass-to-light ratio calculated for AWM 7; our value ($\sim 650 \pm 170 h M_\odot/L_{\odot,R}$ at $0.45 h^{-1}$ Mpc) is concordant with those of similar systems. The mass-to-light ratio approaches the central cD's value at small radii, and is flat at large radii.

The proximity of AWM 7 allows for direct determination of the LF (with redshifts rather than by statistical background subtraction) well below L_* , since L_* corresponds to $R \sim 13$ at 5000 km s^{-1} . A deeper survey will result in denser sampling in the core of the cluster, aiding in discriminating between dynamical models, and will boost the signal in the various tests we have performed here. Deeper surveys will also yield direct measurements of the faint end slope of the LF.

We thank Scott Kenyon and Michael Kurtz for their assistance, and Susan Tokarz for reducing the FAST spectroscopic data. This work is supported by the Smithsonian Institution. DMK was supported by a National Science Foundation Graduate Fellowship.

REFERENCES

- Albert, C., White, R. & Morgan, W., 1977, *ApJ*, 211, 309
- Bacon, R., Monnet, G. & Simien, F., 1985, *A&A*, 152, 315
- Barnes, J., 1992, *ApJ*, 393, 484
- Barnes, J.E. & Hernquist, L., 1992a, *ARA&A*, 30, 705
- Barnes, J.E. & Hernquist, L., 1992b, *Nature*, 360, 715
- Beers, T.C., Geller, M.J., Huchra, J.P., Latham, D.W. & Davis, R.J., 1984, *ApJ*, 283, 33
- Beers, T.C., Kriessler, J.R., Bird, C.M. & Huchra, J.P., 1995, *AJ*, 109, 874
- Bernstein, G.M., Nichol, R.C., Tyson, J.A., Ulmer, M.P., Wittman, D., 1995, *AJ*, 110, 1507
- Binney, J. & Tremaine, S., 1987, *Galactic Dynamics*. Princeton University Press

Biviano, A., Durret, F., Gerbal, D., Le Fèvre, O., Lobo, C., Mazure, A. & Slezak, E., 1995, A&A, 297, 610

Bode, P.W., Berrington, R.C., Cohn, H.N. & Lugger, P.M., 1994, ApJ, 433, 479

Bohlin, R.C., Savage, B.D. & Drake, J.F., 1978, ApJ, 224, 132

Bothun, G.D. & Cornell, M.E., 1990, AJ, 99, 1004

Burstein, D. & Heiles, C., 1978, ApJ, 225, 40

Carlberg, R.G., Yee, H.K.C. & Ellingson, E., 1994, ApJ, 437, 63

Carlberg, R.G., Yee, H.K.C., Ellingson, E., Abraham, R., Gravel, P., Morris, S. & Pritchett, C.J., 1996, ApJ, 462, 32

Carlberg, R.G., Yee, H.K.C. & Ellingson, E., 1997, ApJ, 478, 462

Cavaliere, A. & Fusco-Femiano, R., 1978, A&A, 70, 677

Cirimele, G., Nesci, R. & Trevese, D., 1997, ApJ, 475, 11

Cowie, L.L. & Binney, J., 1977, ApJ, 215, 723

Danese, L., De Zotti, G. & di Tullio, G., 1980, A&A, 82, 322

David, L.P. & Blumenthal, G.R., 1992, ApJ, 389, 510

Dell'Antonio, I.P., Geller, M.J. & Fabricant, D.G., 1995, AJ, 110, 502

den Hartog, R. & Katgert, P., 1996, MNRAS, 279, 349

De Propris, R., Pritchett, C.J., Harris, W.E. & McClure, R.D., 1995, ApJ, 534, 539

Diaconis, P. & Efron, B., 1983, Sci. Am., 248, 116

Diaferio, A., 1997, priv. comm.

Dressler, A. & Shectman, S.A., 1988, AJ, 95, 985

Dubinski, J., 1997, astro-ph/9709102

Efstathiou, G., Ellis, R. S. & Peterson, B. A., 1988, MNRAS, 232, 431

Fabian, A.C., 1994, ARA&A, 32, 277

Fabian, A.C. & Nulsen, P.E.J., 1977, MNRAS, 180, 479

Fabian, A.C., Nulsen, P.E.J. & Canizares, C.R., 1984, MNRAS, 201, 933

Gaidos, E.J., 1997, AJ, 113, 117

Gallagher, J.S. & Ostriker, J.P., 1972, AJ, 77, 288

Geller, M.J., Kurtz, M.J., Wegner, G., Thorstensen, J.R., Fabricant, D.G., Marzke, R.O., Huchra, J.P., Schild, R.E. & Falco, E.E., 1997, AJ, 114, 2205

Kriss, G.A., Canizares, C.R., McClintock, J.E. & Feigelson, E.D., 1980, *ApJ*, 235, L61

Kriss, G.A., Cioffi, D.F. & Canizares, C.R., 1983, *ApJ*, 272, 439

Kurtz, M.J. & Mink, D., 1998, *PASP*, in press (August)

López-Cruz, O., Yee, H.K.C., Brown, J.P., Jones, C. & Forman, W., 1997, *ApJ*, 475, 97L

Malumuth, E.M. & Kirshner, R.P., 1985, *ApJ*, 291, 8

Malumuth, E.M. & Kriss, G.A., 1986, *ApJ*, 308, 10

Marzke, R.O. & da Costa, L.N., 1997, *AJ*, 113, 185

Marzke, R.O., Geller, M.J., Huchra, J.P. & Corwin Jr., H.G., 1994, *AJ*, 108, 437

Merritt, D., 1984, *ApJ*, 276, 26

Merritt, D., 1985, *ApJ*, 289, 18

Mobasher, B. & Trentham, N., 1998, *MNRAS*, 293, 315

Mohr, J.J., Geller, M.J., Fabricant, D.G., Wegner, G., Thorstensen, J. & Richstone, D.O., 1996a, *ApJ*, 470, 724

Mohr, J.J., Geller, M.J. & Wegner, G., 1996b, *AJ*, 112, 1816

Morgan, W.W., Kayser, S. & White, R.A., 1975, *ApJ*, 199, 545

Navarro, J.F., Frenk, C.S. & White, S.D.M., 1995, *MNRAS*, 275, 720

Navarro, J.F., Frenk, C.S. & White, S.D.M., 1997, *ApJ*, 490, 493

Neumann, D.M. & Böhringer, H., 1995, *A&A*, 301, 865 (NB)

Oemler, A., 1976, *ApJ*, 440, 28

Ostriker, J.P. & Tremaine, S., 1975, *ApJ*, 202, L113

Ostriker, J.P. & Hausmann, M.A., 1977, *ApJ*, 217, L125

Press, W.H., Flannery, B.P., Teukolsky, S.A. & Vetterling, W.T., 1992, *Numerical Recipes: The Art of Scientific Computing (Fortran Version)*. 2nd ed. Cambridge University Press

Price, R., Burns, J.O., Duric, N. & Newberry, M.V., 1991, *AJ*, 102, 14

Richstone, D., 1975, *ApJ*, 200, 535

Richstone, D., 1976, *ApJ*, 204, 642

Schechter, P., 1976, *ApJ*, 203, 297

Sprayberry, D., Impey, C.D., Irwin, M.J. & Bothun, G.D., 1997, *ApJ*, 482, 104

Stark, A.A., Gammie, C.F., Wilson, R.W., Bally, J., Linke, R.A. Heiles, C. & Hurwitz, M., 1992, ApJS, 79, 77

The, L.S. & White, S.D.M., 1986, AJ, 92, 1248

Trentham, N., 1997, MNRAS, 286, 133

Tyson, J.A. & Fischer, P., 1995, ApJ, 446, L55

White, S.D.M., 1976, MNRAS, 174, 19

Williams, B.A. & Lynch, J.R., 1991, AJ, 101, 1969

Wilson, G., Smail, I., Ellis, R.S. & Couch, W.J., 1997, MNRAS, 284, 915

Zombeck, M.V., 1992, *Handbook of Space Astronomy and Astrophysics* 2nd. ed. Cambridge University Press

Zwicky, F., Herzog, E., Wild, P., Karpowicz, M. & Kowal, C.T., 1962, *Catalog of Galaxies and Clusters of Galaxies* (Pasadena: California Institute of Technology)

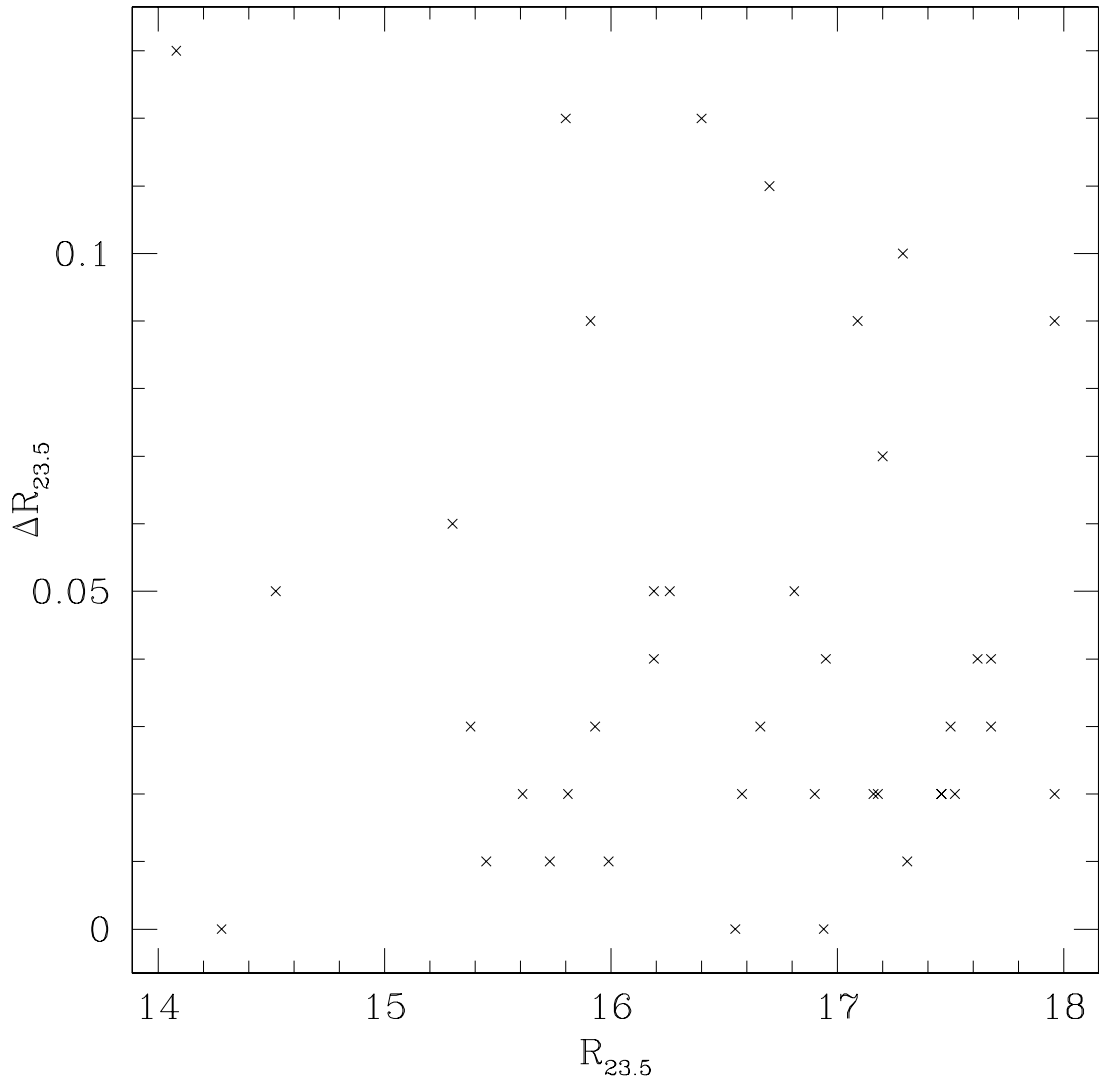


Fig. 1.— Absolute value of the difference in magnitudes determined from separate mosaic fields, for galaxies (in overlap regions) with multiple magnitude measurements. Each such galaxy generates one point on this plot; we plot the greatest magnitude difference against the brightest magnitude.

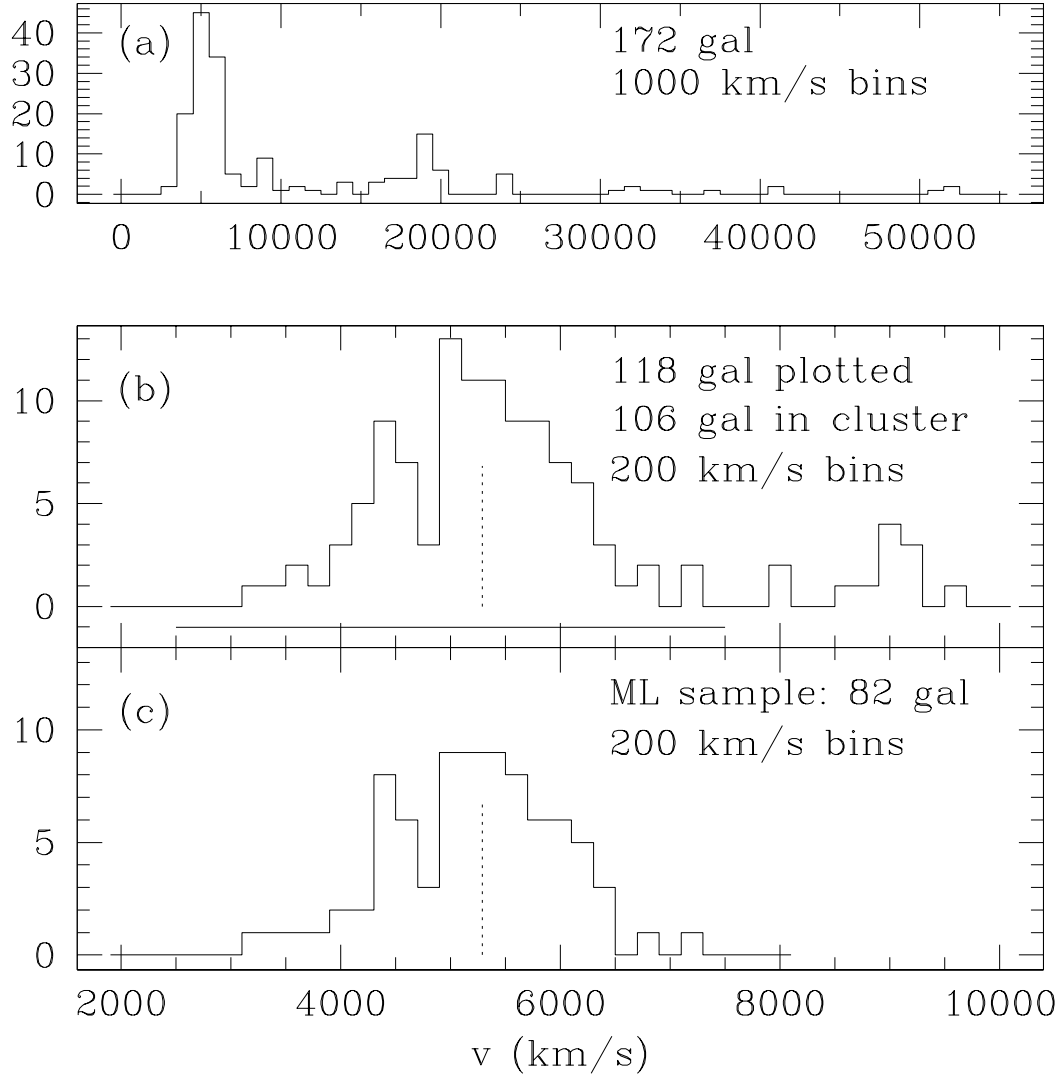


Fig. 2.— (a) Velocity distribution of the 176 galaxies with measured redshifts. (b) Velocity distribution of galaxies with $cz < 10000$ km s $^{-1}$. The solid rule beneath the histogram indicates the velocity criterion for cluster membership. (c) The velocity distribution of the 82 galaxies with $2500 < v < 7500$ km s $^{-1}$ and with CCD photometry that constitute the core sample. In (b) and (c) the velocity of the central cD galaxy is indicated by the dotted line.

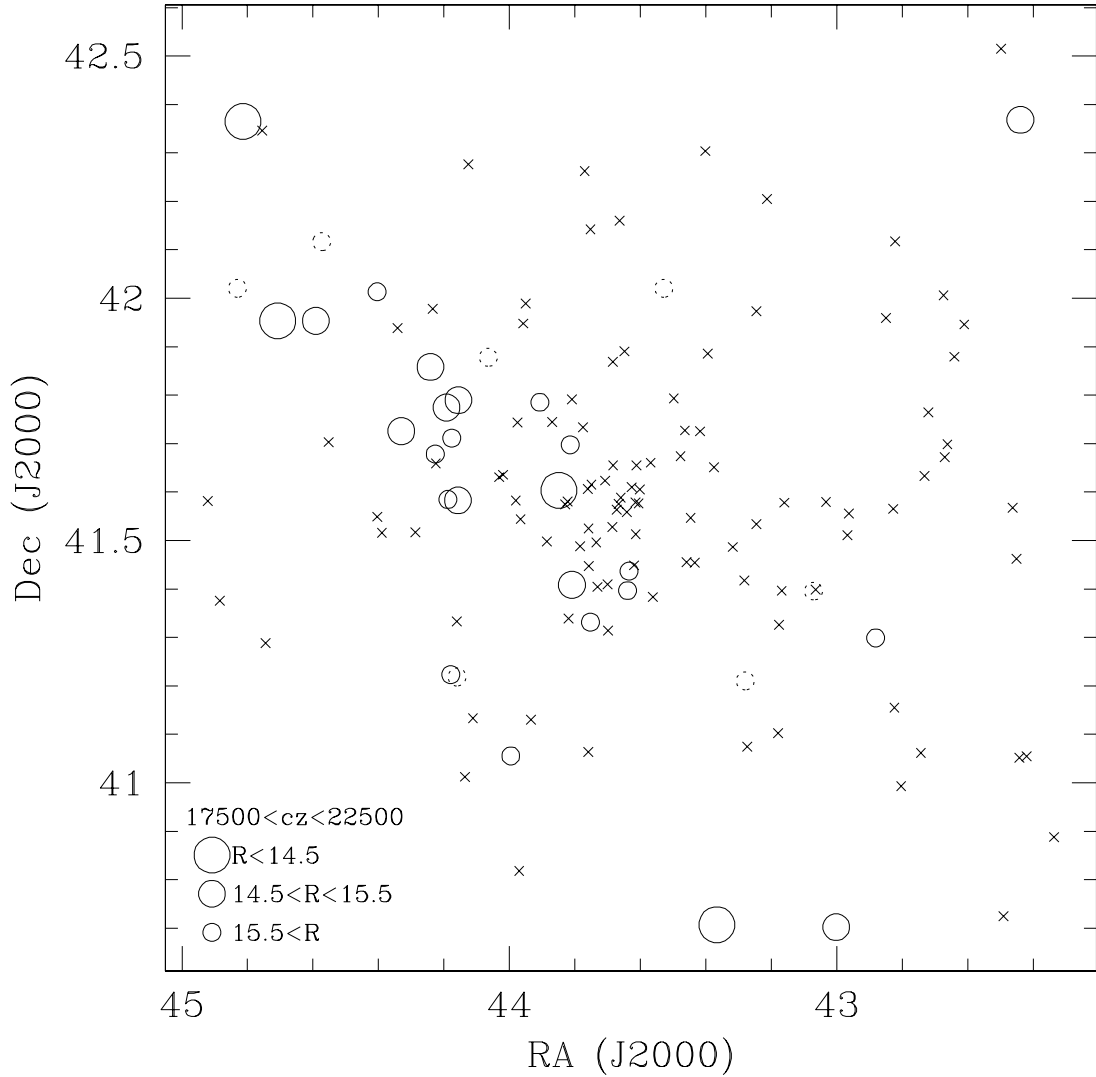


Fig. 3.— The angular distribution of the clusters and background structure. Crosses are galaxies in AWM 7, with $2500 < cz < 7500$ km s^{-1} . Dashed circles are background galaxies with $15000 < cz \leq 17500$ km s^{-1} . Solid circles are background galaxies with $17500 < cz < 22500$ km s^{-1} , coded by size for magnitude.

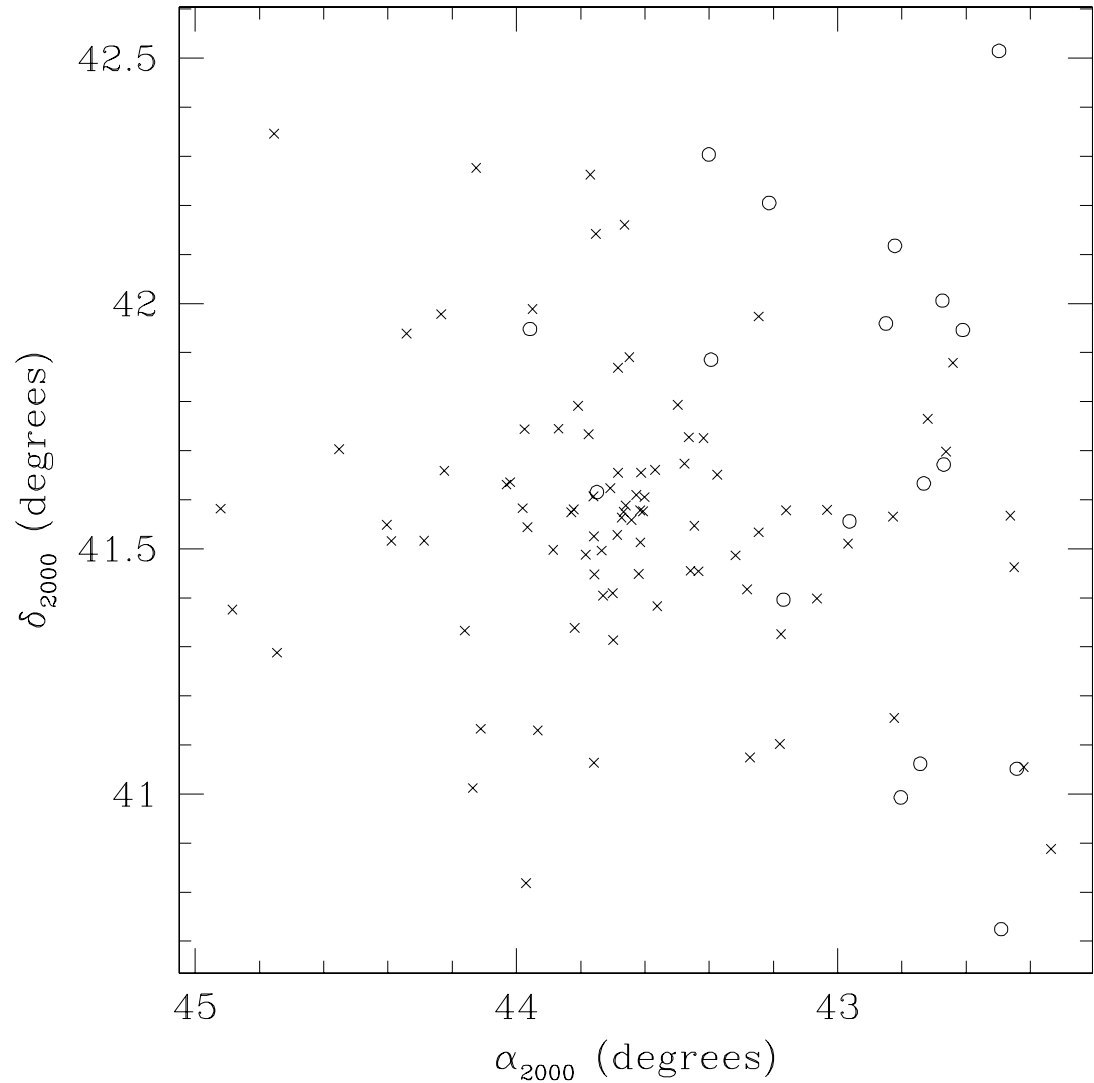


Fig. 4.— The angular distribution of the 106 C galaxies with $2500 < v < 7500$ km s⁻¹, both within and without the region with CCD photometry. Emission-line galaxies are circles; non-emission galaxies are crosses.

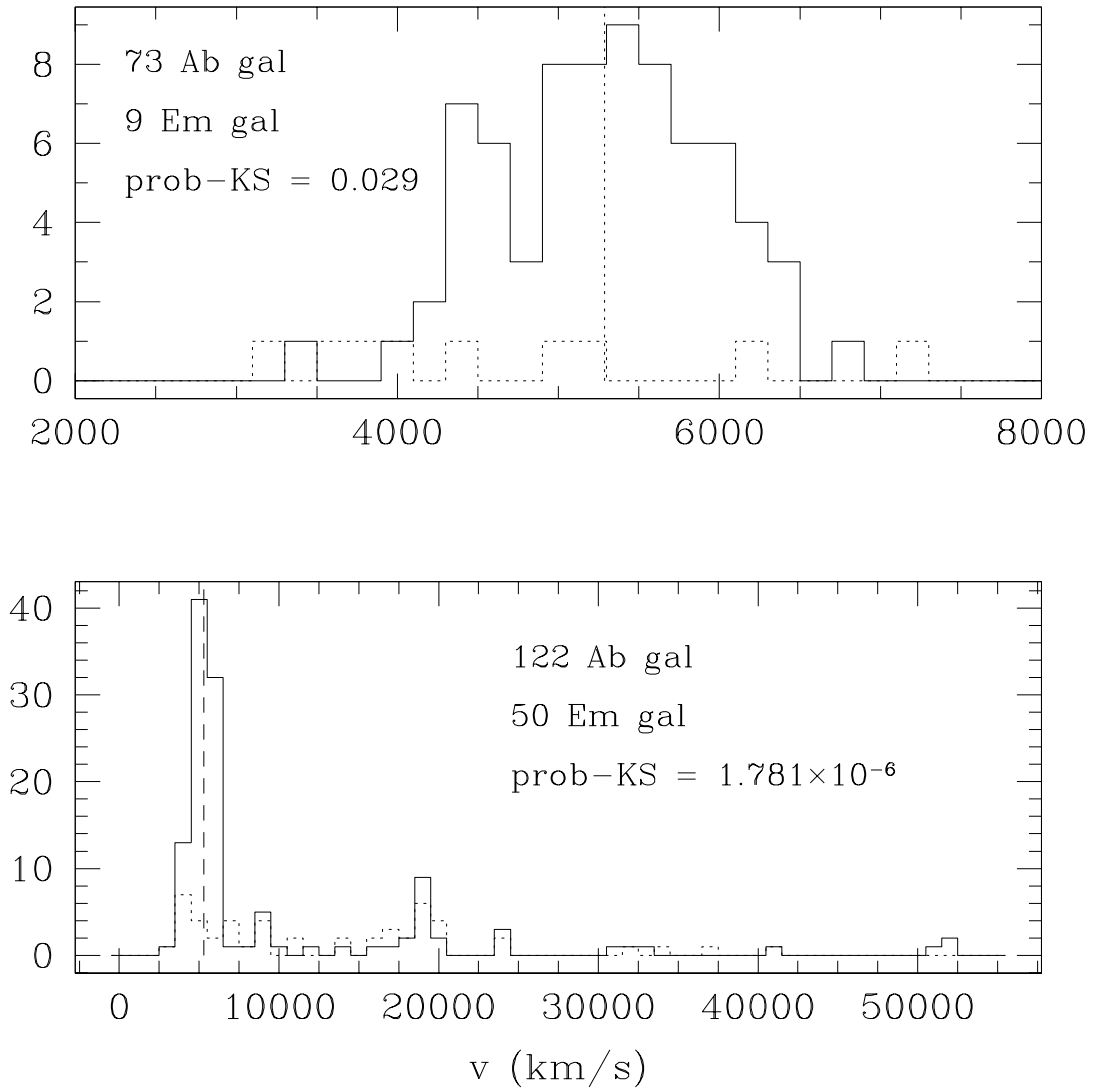


Fig. 5.— Velocity distribution of the emission and non-emission galaxies. The upper panels show only galaxies in the ML sample with CCD photometry. The central cD's velocity is indicated with a dotted line in each panel.

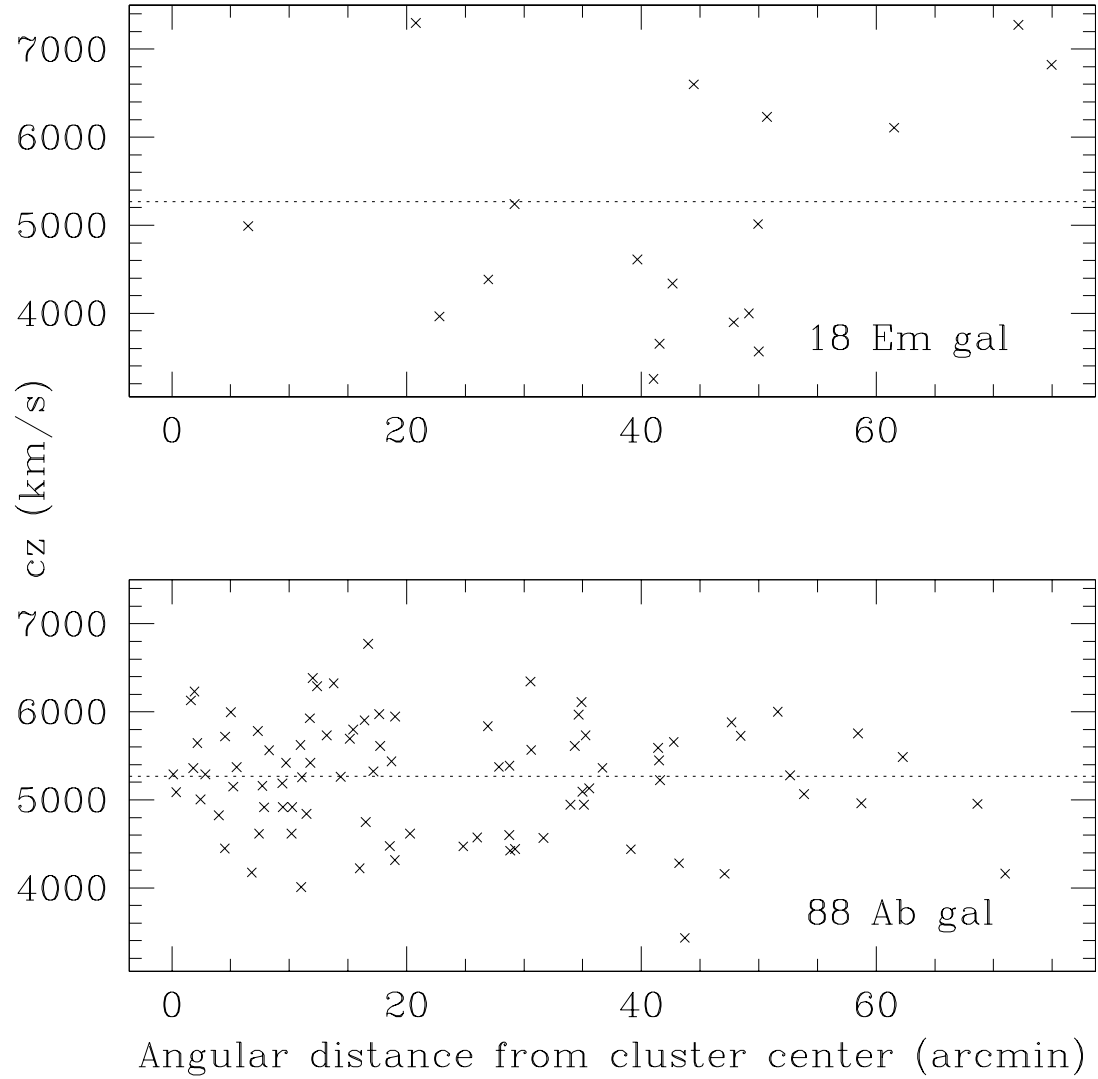


Fig. 6.— Radial velocity as a function of angular distance from the central cD for the Em and Ab galaxies in the C sample. The dotted line indicates the mean cluster redshift.

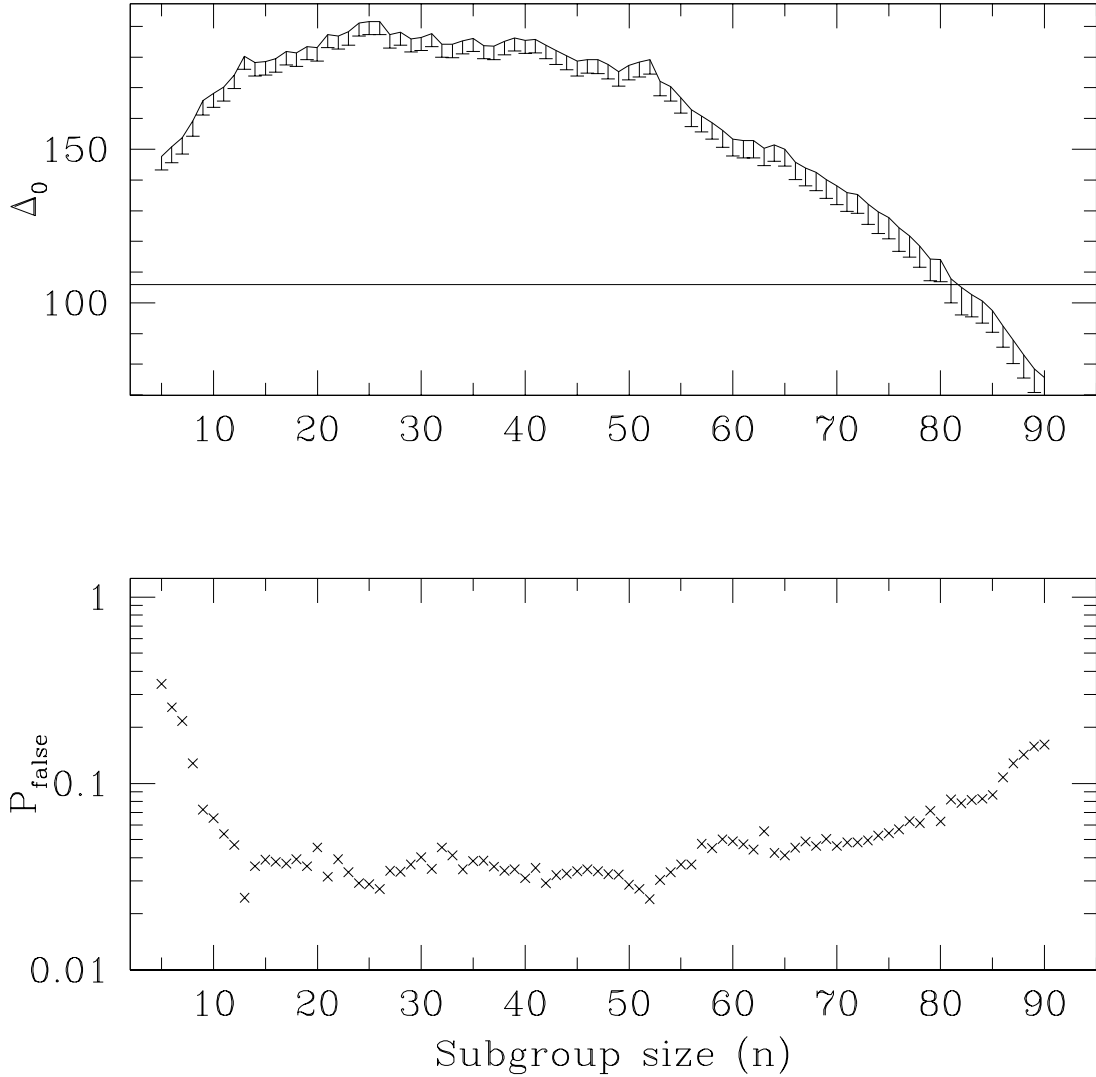


Fig. 7.— Top: the Dressler-Shectman statistic Δ_0 as a function of subgroup size n . The horizontal rule is at $\Delta_0 = 106$, the (Em+Ab) sample size. Bottom: the probability of Δ_0 being equal to or greater than the observed value by chance, as derived from 5000 Monte Carlo simulations.

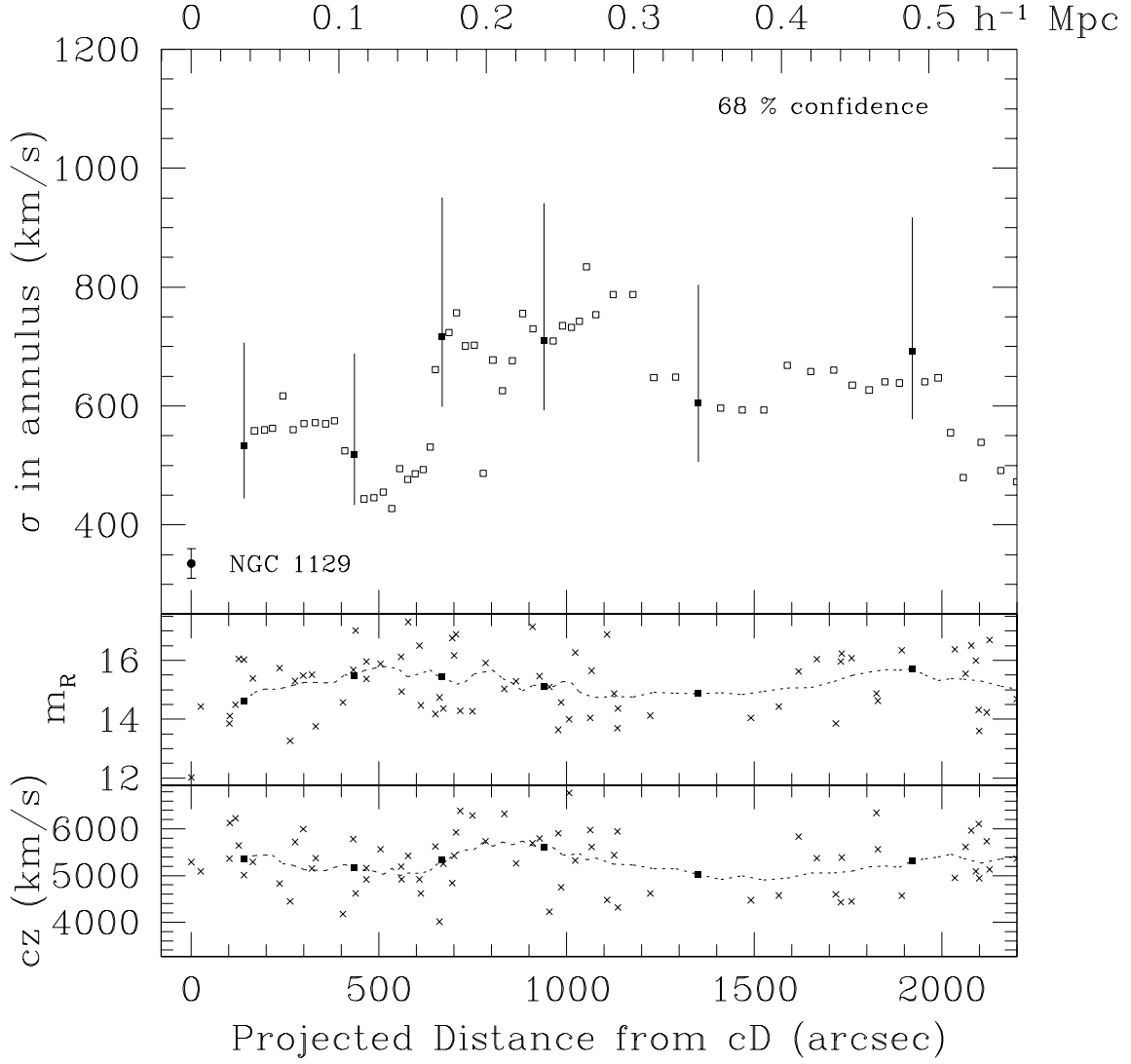


Fig. 8.— Velocity dispersion, apparent magnitude, and velocity of Ab-type galaxies as a function of projected cluster radius. σ and median values of m_R and cz (dotted lines) are calculated from a sliding bin of 11 galaxies; independent (uncorrelated) points are filled squares, with 68% error bars for $\sigma(r)$. Data point for N1129 represents internal σ of galaxy. In the lower panels, crosses denote individual galaxies.

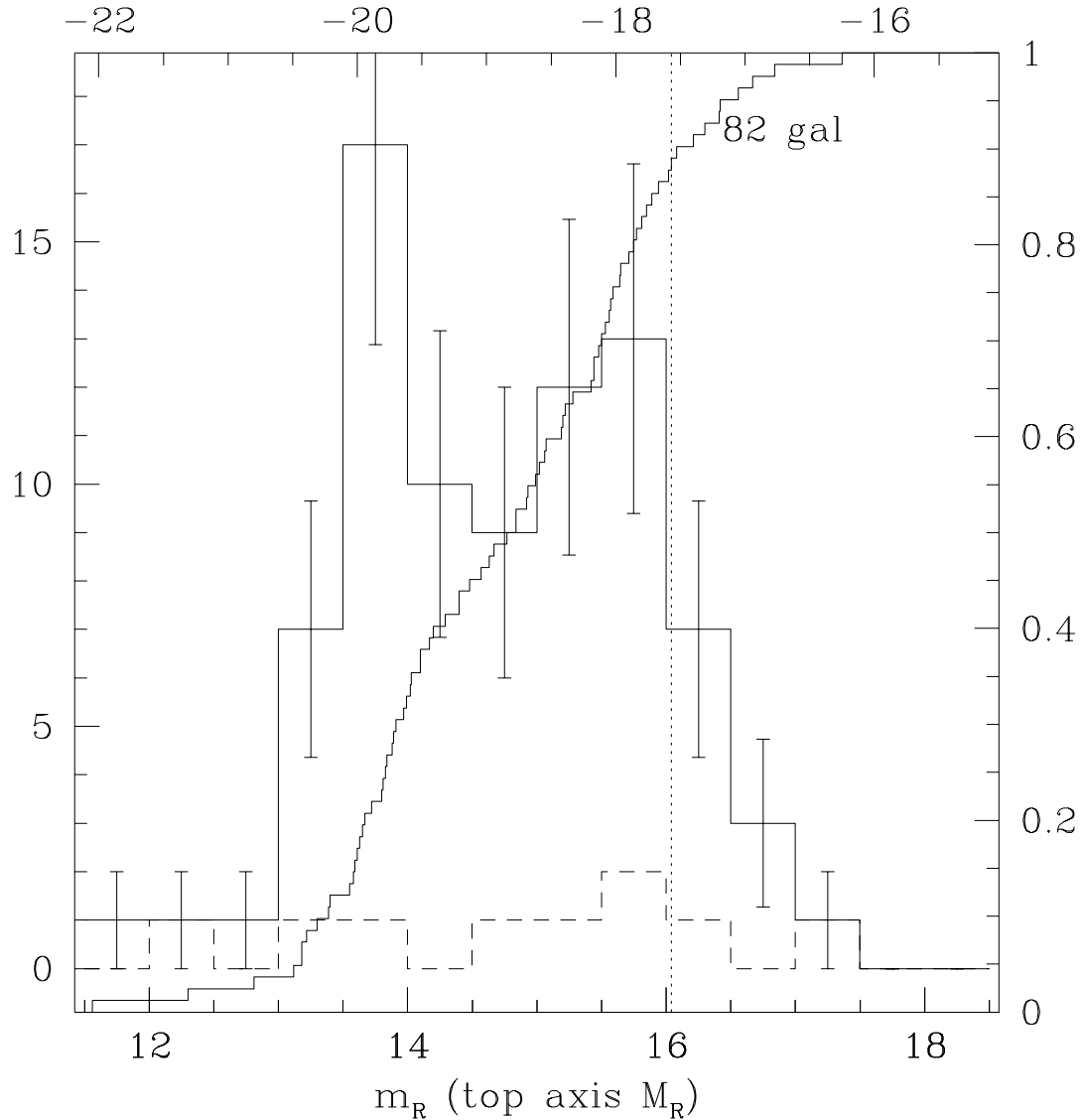


Fig. 9.— The differential (left-hand scale) and cumulative (right-hand scale) extinction-corrected apparent magnitude distributions for the ML sample. Errors on the histogram are \sqrt{N} .

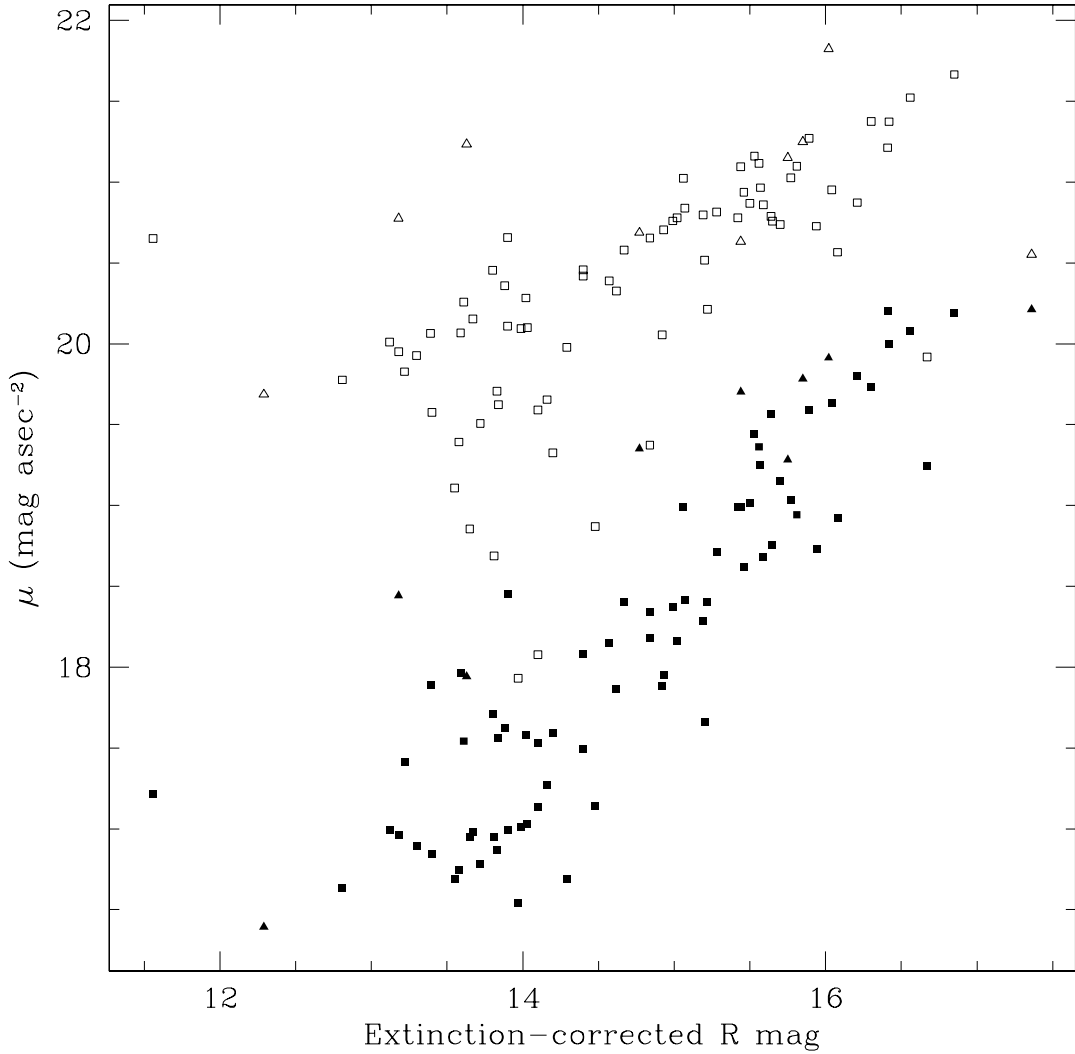


Fig. 10.— Mean (open) and central (solid) surface brightness for the 82 sample galaxies. The central surface brightness is determined in the 3×3 pixel grid with the highest flux, corresponding to a patch $1''.33$ square on the sky. Em galaxies are plotted as triangles; Ab galaxies as squares.

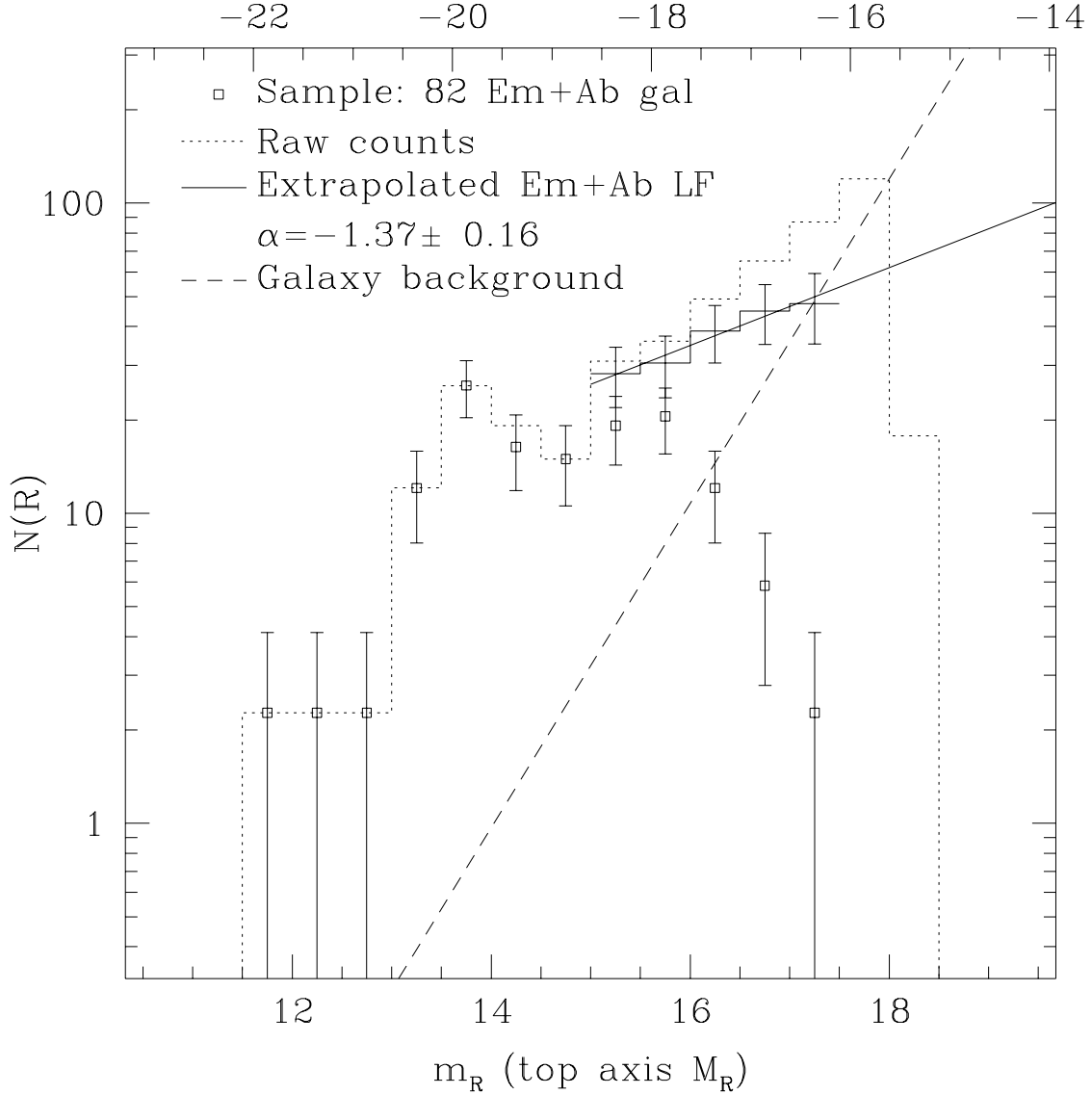


Fig. 11.— Raw galaxy counts (dotted histogram), sample galaxy counts (points with error bars), $10^{0.6m}$ background (dashed line), and extrapolated LF (solid histogram and line). The best power-law fit to the extrapolated LF corresponds to $\alpha = -1.36 \pm 0.16$ in the Schechter parametrization. The completeness limit is 16.0 .

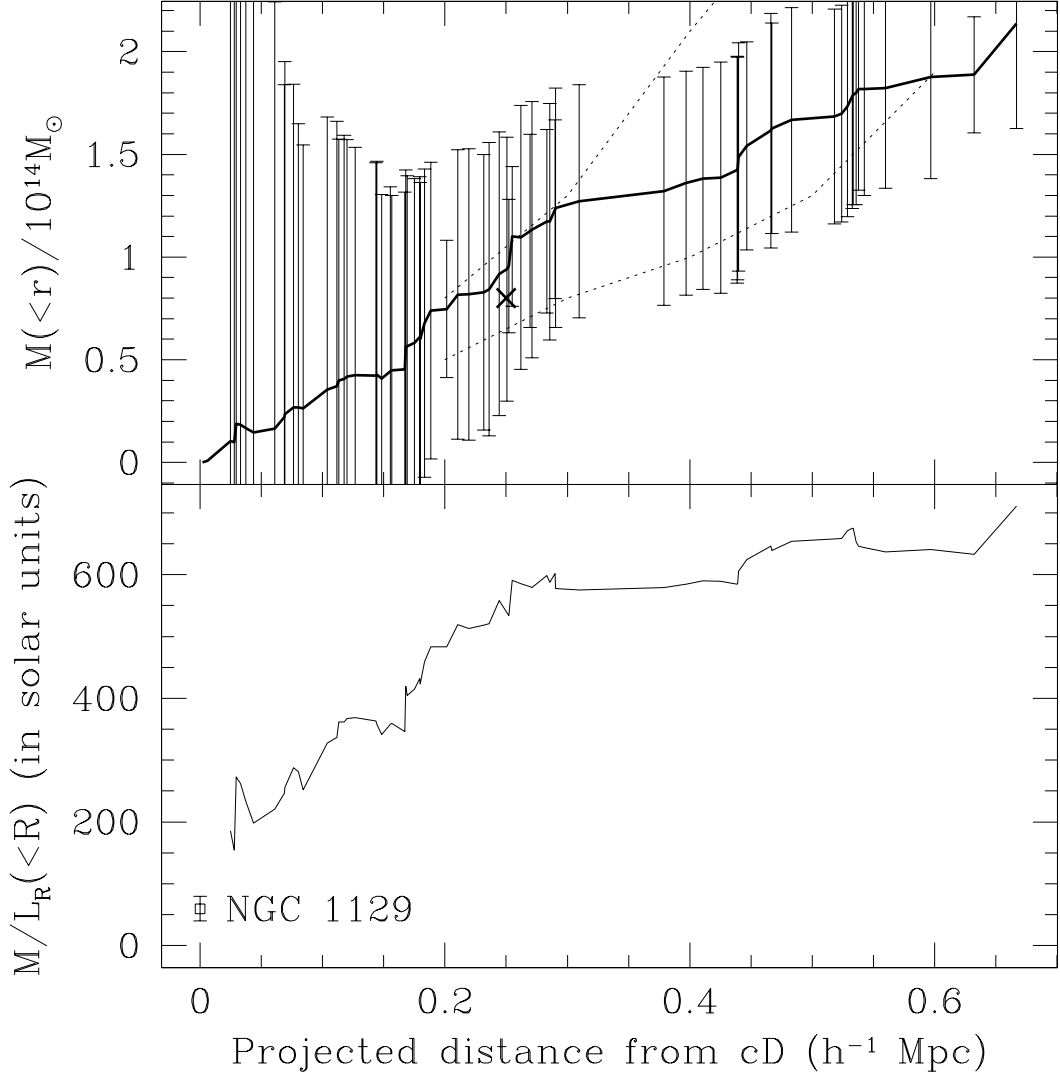


Fig. 12.— The enclosed virial mass (top) and R -band mass-to-light ratio (bottom) as a function of projected radius in the cluster. The \times marks the data point from Dell'Antonio *et al.* (1995); the dotted lines indicate the profile of NB. Errors on the mass are statistical jackknife estimates; they scale uniformly to errors on M/L . The data point for NGC 1129 is from Bacon *et al.* (1985). Note that $M/L_B = 1.58 M/L_R$ for Em galaxies with $B-R = 1.5$, and that $M/L \propto h$.

Table 1. Properties of Sample Galaxies

α_{2000}	δ_{2000}	cz	σ_{cz}	m_R	Δm_R	phot	Em-type	A_R
2 49 20.60	40 53 17.02	4161	31.4	14.99	0.250	P	Ab	0.40
2 49 40.90	41 03 17.00	5489	31.3	14.42	0.250	P	Ab	0.41
2 49 45.30	42 22 05.81	19811	21.2	15.45	0.250	P	Em*	0.45
2 49 45.90	41 27 26.10	24087	44.0	14.98	0.250	P	Em	0.42
2 49 46.10	41 03 06.00	6108	19.0	13.48	0.250	P	Em*	0.41
2 49 48.10	41 27 45.50	5279	17.0	13.13	0.250	P	Ab	0.42
2 49 51.00	41 34 03.70	6000	28.8	13.80	0.250	P	Ab	0.42
2 49 57.80	40 43 28.31	7276	19.8	15.14	0.250	P	Em*	0.40
2 49 59.40	42 30 53.71	6824	25.6	15.45	0.250	P	Em*	0.46
2 50 26.50	41 56 45.38	5014	28.0	14.78	0.250	P	Em	0.44
2 50 33.80	41 52 45.30	4160	50.2	14.85	0.250	P	Ab	0.44
2 50 38.90	41 41 54.49	4281	21.9	14.62	0.250	P	Ab	0.43
2 50 40.70	41 40 18.30	4337	19.2	13.63	0.250	P	Em*	0.43
2 50 41.70	42 00 21.10	4000	18.6	14.46	0.250	P	Em	0.44
2 50 52.80	41 45 52.70	5449	62.5	15.35	0.250	P	Ab	0.44
2 50 55.60	41 37 59.90	4611	16.3	13.63	0.250	P	Em	0.43
2 50 58.30	41 03 42.80	3567	20.3	14.30	0.250	P	Em*	0.42
2 51 04.94	41 42 06.81	23984	36.8	17.84	0.071	25	Ab	0.44
2 51 12.58	41 02 09.41	9016	19.9	16.64	0.062	22	Ab	0.42
2 51 12.80	40 59 35.48	6229	20.1	16.44	0.062	22	Em*	0.42
2 51 17.20	42 07 03.79	3898	32.5	16.30	0.068	27	Em*	0.45
2 51 17.70	41 09 18.40	3433	21.3	15.09	0.062	22	Ab	0.42
2 51 18.60	41 33 55.10	5734	34.4	14.23	0.065	24	Ab	0.43
2 51 23.90	41 57 33.60	3256	18.1	15.22	0.064	26	Em*	0.45
2 51 29.30	40 44 26.81	8096	24.7	15.61	0.250	P	Ab	0.41
2 51 31.37	41 17 57.00	20476	19.5	16.13	0.062	23	Em*	0.43
2 51 33.50	40 46 27.08	41276	44.0	15.63	0.250	P	Ab	0.42
2 51 34.50	40 43 53.40	8900	35.9	14.28	0.250	P	Ab	0.41
2 51 36.35	41 22 56.06	9519	20.9	16.55	0.062	23	Ab	0.43
2 51 37.80	40 44 24.10	8077	18.4	14.17	0.250	P	Em	0.42
2 51 41.10	42 21 51.98	11192	22.1	15.21	0.250	P	Em*	0.47
2 51 42.80	42 24 09.00	11312	17.9	14.21	0.250	P	Em*	0.47
2 51 51.10	41 33 21.31	5241	54.4	16.19	0.065	24	Em	0.44
2 51 52.26	41 30 38.88	4444	130.5	16.08	0.065	24	Ab	0.44
2 52 00.40	40 42 07.81	18137	37.6	15.24	0.250	P	Ab	0.42
2 52 07.90	41 34 45.90	4573	17.0	14.43	0.065	24	Ab	0.44
2 52 08.60	41 14 47.29	23852	36.9	16.54	0.062	23	Ab	0.43
2 52 15.50	41 23 55.10	5836	23.8	15.63	0.062	34	Ab	0.44
2 52 16.99	41 23 44.36	17084	21.9	16.31	0.062	34	Ab	0.44
2 52 25.90	41 53 00.89	8619	28.3	15.57	0.062	36	Em*	0.45
2 52 38.50	41 34 41.10	4619	20.1	14.12	0.062	34	Ab	0.45

Table 1—Continued

α_{2000}	δ_{2000}	cz	σ_{cz}	m_R	Δm_R	phot	Em-type	A_R
2 52 40.40	41 23 46.50	3964	15.5	14.07	0.062	34	Em*	0.44
2 52 42.00	41 48 48.60	34212	15.2	17.09	0.062	36	Em	0.45
2 52 42.30	41 19 33.50	4472	53.9	14.05	0.062	33	Ab	0.44
2 52 43.10	41 06 08.76	5968	31.7	16.51	0.062	32	Ab	0.43
2 52 45.00	42 09 44.89	32900	32.7	16.46	0.062	37	Ab	0.46
2 52 46.00	41 00 22.11	30934	33.5	16.44	0.062	32	Ab	0.43
2 52 51.20	42 12 18.10	3655	18.3	12.77	0.062	37	Em*	0.47
2 52 58.90	41 32 01.60	6771	25.5	14.00	0.062	34	Ab	0.45
2 52 59.00	41 58 24.71	5388	26.3	16.23	0.062	36	Ab	0.46
2 53 00.70	41 06 27.00	9178	32.1	16.42	0.062	32	Em*	0.44
2 53 00.80	40 50 23.60	9154	32.3	14.32	0.250	P	Em	0.43
2 53 03.50	41 17 25.80	14376	19.6	16.61	0.062	33	Em*	0.44
2 53 05.61	41 04 27.94	4947	24.4	16.38	0.062	32	Ab	0.44
2 53 07.00	41 12 37.91	15993	24.6	15.70	0.062	33	Em*	0.44
2 53 07.70	41 25 03.68	5614	32.3	15.65	0.062	34	Ab	0.45
2 53 14.10	41 45 21.60	50734	44.7	16.83	0.062	35	Ab	0.46
2 53 16.20	41 29 11.80	5262	26.3	15.29	0.062	34	Ab	0.45
2 53 16.80	41 27 58.21	23928	37.8	16.65	0.062	34	Ab	0.45
2 53 27.90	40 42 25.09	18365	35.6	14.33	0.250	P	Em	0.43
2 53 28.35	42 05 09.45	41148	119.9	16.25	0.054	47	Em	0.47
2 53 30.00	41 39 03.38	4840	31.9	16.76	0.054	45	Ab	0.46
2 53 34.60	41 53 08.10	7298	14.0	13.64	0.054	46	Em*	0.46
2 53 36.30	42 18 13.70	6600	19.5	13.93	0.250	P	Em	0.48
2 53 40.20	41 43 31.10	6291	28.1	14.27	0.054	45	Ab	0.46
2 53 44.10	41 27 15.08	4010	31.8	14.74	0.062	44	Ab	0.45
2 53 47.10	41 32 49.09	5161	31.4	15.37	0.062	44	Ab	0.45
2 53 50.00	41 27 18.40	4617	44.5	14.47	0.062	44	Ab	0.45
2 53 51.30	41 43 38.20	5257	17.6	14.37	0.054	45	Ab	0.46
2 53 54.50	41 40 25.61	5562	48.8	15.88	0.054	45	Ab	0.46
2 53 59.50	41 47 35.09	6325	22.9	15.03	0.054	45	Ab	0.46
2 54 06.70	42 01 14.81	17174	26.2	16.28	0.054	47	Em	0.47
2 54 11.80	40 58 46.42	9176	71.2	17.90	0.062	42	Ab	0.44
2 54 14.80	41 23 00.00	6386	23.4	14.28	0.062	44	Ab	0.45
2 54 16.40	41 39 38.41	5151	29.8	15.52	0.054	45	Ab	0.46
2 54 24.40	41 36 19.40	6130	25.9	14.11	0.054	45	Ab	0.46
2 54 25.28	41 34 35.77	5089	17.3	14.43	0.062	44	Ab	0.46
2 54 26.85	41 39 19.33	5720	14.0	15.30	0.054	55	Ab	0.46
2 54 27.40	41 30 47.30	4827	72.8	15.74	0.054	54	Ab	0.46
2 54 27.50	41 34 42.50	5288	70.6	12.02	0.054	54	Ab	0.46
2 54 28.57	41 26 55.94	4916	22.9	15.96	0.054	54	Ab	0.46
2 54 30.40	41 36 36.22	6231	23.6	14.49	0.054	55	Ab	0.46

Table 1—Continued

α_{2000}	δ_{2000}	cz	σ_{cz}	m_R	Δm_R	phot	Em-type	A_R
2 54 32.20	41 26 11.90	19756	40.8	16.52	0.054	54	Ab	0.46
2 54 32.40	42 23 41.21	23731	38.5	15.12	0.250	P	Em*	0.49
2 54 33.30	41 23 48.30	19366	55.1	16.72	0.054	54	Ab	0.46
2 54 34.01	41 33 31.27	5361	17.4	13.86	0.054	54	Ab	0.46
2 54 35.70	41 53 25.19	5438	22.0	14.87	0.054	56	Ab	0.47
2 54 38.30	41 35 18.10	5646	26.4	16.05	0.054	55	Ab	0.46
2 54 39.25	42 09 36.93	6111	16.2	14.32	0.054	57	Ab	0.48
2 54 40.00	41 34 31.12	5007	39.2	16.03	0.054	54	Ab	0.46
2 54 41.40	41 33 49.28	5291	44.9	15.39	0.054	54	Ab	0.46
2 54 44.00	41 39 18.00	5372	24.6	13.76	0.054	55	Ab	0.46
2 54 44.10	41 52 08.80	5974	23.9	14.05	0.054	56	Ab	0.47
2 54 44.60	41 31 41.40	4450	22.1	13.27	0.054	54	Ab	0.46
2 54 47.60	41 18 50.00	5905	40.1	13.64	0.054	53	Ab	0.46
2 54 48.10	41 24 34.00	5622	16.5	14.18	0.054	54	Ab	0.46
2 54 49.80	41 37 25.39	5995	37.8	15.48	0.054	55	Ab	0.46
2 54 55.30	41 24 15.41	5423	41.7	16.17	0.054	54	Ab	0.46
2 54 56.30	41 29 46.79	4615	40.7	17.02	0.054	54	Ab	0.46
2 54 59.90	41 36 56.09	4991	20.9	17.83	0.054	55	Em*	0.47
2 55 00.60	41 19 53.29	19842	60.1	16.52	0.054	53	Em	0.46
2 55 00.60	42 08 32.00	5614	26.1	15.55	0.054	57	Ab	0.48
2 55 01.80	41 26 51.30	4918	51.2	16.50	0.054	54	Ab	0.46
2 55 02.00	41 31 30.40	5782	22.1	15.68	0.054	54	Ab	0.46
2 55 02.13	41 03 49.45	4567	41.2	16.34	0.054	52	Ab	0.45
2 55 02.40	41 36 24.10	4176	18.4	14.57	0.054	55	Ab	0.47
2 55 04.80	42 15 45.80	5224	22.9	14.30	0.250	P	Ab	0.49
2 55 06.00	41 44 00.38	5927	53.1	16.89	0.054	55	Ab	0.47
2 55 08.20	41 29 17.09	4918	40.5	14.94	0.054	54	Ab	0.46
2 55 14.10	41 24 30.71	19663	32.4	15.75	0.054	54	Em	0.46
2 55 14.10	41 47 29.80	5798	51.8	15.46	0.054	56	Ab	0.47
2 55 15.40	41 41 51.79	18463	36.6	16.71	0.054	55	Ab	0.47
2 55 16.60	41 20 20.51	5325	30.8	16.27	0.054	53	Ab	0.46
2 55 17.33	41 34 49.01	5188	24.5	16.12	0.054	54	Ab	0.47
2 55 19.01	41 34 28.02	5422	21.4	17.31	0.054	54	Ab	0.47
2 55 23.70	41 36 12.82	18501	36.6	14.72	0.054	55	Ab	0.47
2 55 28.58	41 44 40.95	5696	18.0	17.14	0.054	55	Ab	0.47
2 55 32.50	41 29 53.30	5735	49.4	15.91	0.054	54	Ab	0.47
2 55 36.74	41 51 33.55	31907	460.3	16.81	0.054	66	Ab	0.48
2 55 37.50	42 02 05.61	37186	42.2	16.99	0.054	67	Em*	0.48
2 55 37.70	41 47 07.40	18733	20.3	18.45	0.054	65	Em*	0.48
2 55 44.03	41 07 48.05	5567	17.3	14.63	0.054	62	Ab	0.46
2 55 44.13	41 36 51.27	14366	14.9	16.78	0.054	65	Ab	0.47

Table 1—Continued

α_{2000}	δ_{2000}	cz	σ_{cz}	m_R	Δm_R	phot	Em-type	A_R
2 55 48.00	41 59 20.11	4423	23.2	15.96	0.054	66	Ab	0.48
2 55 49.90	41 56 52.40	4385	27.9	15.92	0.054	66	Em*	0.48
2 55 51.80	41 32 39.01	4224	76.9	15.10	0.054	64	Ab	0.47
2 55 52.80	40 49 05.59	5728	31.5	15.07	0.250	P	Ab	0.45
2 55 54.00	41 44 37.60	4317	94.5	14.37	0.054	65	Ab	0.48
2 55 55.30	41 34 58.10	4749	26.9	14.57	0.054	65	Ab	0.47
2 55 58.97	41 03 20.10	19611	22.8	16.61	0.054	62	Ab	0.46
2 56 04.61	41 38 08.74	4477	29.9	16.88	0.054	65	Ab	0.47
2 56 07.40	41 37 51.10	5948	26.1	13.69	0.054	65	Ab	0.47
2 56 15.51	41 52 40.80	15891	20.7	16.55	0.054	66	Em*	0.48
2 56 26.70	41 07 59.09	5092	41.2	15.99	0.054	62	Ab	0.46
2 56 30.10	42 16 35.90	5882	53.2	15.27	0.250	P	Ab	0.50
2 56 32.60	41 00 44.30	5592	23.5	14.34	0.054	62	Ab	0.46
2 56 37.40	41 47 23.50	18766	55.6	15.80	0.054	75	Em	0.48
2 56 37.70	41 34 58.69	18585	26.4	15.75	0.054	65	Ab	0.48
2 56 38.43	41 13 05.63	16621	21.4	16.23	0.054	73	Em*	0.47
2 56 38.60	41 19 59.82	4601	17.4	13.86	0.054	73	Ab	0.47
2 56 42.25	41 42 41.35	18509	30.2	16.00	0.054	75	Ab	0.48
2 56 43.03	41 13 24.29	18628	23.5	16.81	0.054	73	Ab	0.47
2 56 45.10	41 35 04.90	18758	23.1	16.57	0.054	75	Ab	0.48
2 56 46.12	41 46 28.76	18475	39.1	15.52	0.054	75	Em*	0.48
2 56 53.90	41 39 33.19	5375	44.9	16.04	0.054	75	Ab	0.48
2 56 54.39	41 40 42.24	18674	26.2	16.41	0.054	75	Ab	0.48
2 56 56.03	41 20 49.54	51638	40.9	16.54	0.054	73	Ab	0.47
2 56 56.20	41 58 41.90	5364	22.1	14.69	0.054	76	Ab	0.49
2 56 56.40	40 48 14.40	14424	15.1	14.85	0.250	P	Em	0.45
2 56 57.87	41 51 29.67	18822	20.6	15.94	0.054	76	Ab	0.49
2 57 08.97	41 31 00.20	6344	30.6	14.88	0.054	74	Ab	0.48
2 57 19.20	41 43 33.31	18789	52.7	15.95	0.054	75	Em	0.49
2 57 22.00	41 56 19.50	4439	20.4	14.08	0.054	76	Ab	0.49
2 57 33.50	41 30 57.90	4944	20.8	13.60	0.054	74	Ab	0.48
2 57 36.79	41 32 56.89	5131	22.7	16.69	0.054	74	Ab	0.48
2 57 36.87	42 00 47.71	19258	30.2	16.24	0.054	77	Em*	0.50
2 57 37.26	41 33 27.57	51515	60.6	16.97	0.054	74	Ab	0.48
2 57 37.50	42 00 31.67	31986	41.4	16.91	0.054	77	Em	0.50
2 57 41.56	41 56 26.47	11595	17.4	15.61	0.054	76	Ab	0.50
2 58 12.40	41 42 11.90	5659	26.2	14.52	0.250	P	Ab	0.49
2 58 17.60	42 06 59.80	16254	26.8	15.18	0.250	P	Ab	0.51
2 58 21.90	41 57 12.60	18763	33.5	15.04	0.250	P	Em*	0.51
2 58 31.50	40 51 39.10	9049	37.8	14.37	0.250	P	Ab	0.47
2 58 37.60	40 52 06.40	9089	27.9	14.68	0.250	P	Ab	0.47

Table 1—Continued

α_{2000}	δ_{2000}	cz	σ_{cz}	m_R	Δm_R	phot	Em-type	A_R
2 58 49.80	41 57 12.60	18536	45.3	14.77	0.250	P	Ab	0.51
2 58 54.10	40 44 57.70	9038	15.2	14.40	0.250	P	Em	0.47
2 58 58.80	41 17 17.50	5066	25.1	13.96	0.250	P	Ab	0.49
2 59 01.10	42 20 45.50	4954	21.9	13.86	0.250	P	Ab	0.53
2 59 15.30	42 21 54.11	19054	42.5	14.89	0.250	P	Em*	0.54
2 59 19.30	42 01 13.91	16536	22.3	15.54	0.250	P	Em*	0.52
2 59 32.20	41 22 32.80	5754	20.4	14.18	0.250	P	Ab	0.50
2 59 41.10	41 34 54.80	4962	38.7	15.19	0.250	P	Ab	0.50

Note. — Column 1 lists the galaxy RA; column 2, the declination; column 3, the radial velocity; column 4, the uncertainty in the radial velocity; column 5, the isophotal magnitude (to 23.5 mag asec $^{-2}$ in R_{KC}); column 6, the error in isophotal magnitude; column 7, the source of the magnitude (CCD frame number or P for POSS); column 8, the spectral type (presence or absence of H α emission, quantified in §3); and column 9, the extinction A_R along the line of sight to the galaxy.